Geometrically motivated coordinate system for exploring spacetime dynamics in numerical-relativity simulations using a quasi-Kinnersley tetrad

Fan Zhang,[1] Jeandrew Brink,[2] Béla Szilágyi,[1] and Geoffrey Lovelace[3]

[1]*Theoretical Astrophysics 350-17, California Institute of Technology, Pasadena, California 91125, USA*
[2]*National Institute of Theoretical Physics, Private Bag X1 Matieland, Stellenbosch 7602, South Africa*
[3]*Center for Radiophysics and Space Research, Cornell University, Ithaca, New York 14853, USA*

(Received 2 August 2012; published 3 October 2012)

We investigate the suitability and properties of a quasi-Kinnersley tetrad and a geometrically motivated coordinate system as tools for quantifying both strong-field and wave-zone effects in numerical relativity (NR) simulations. We fix two of the coordinate degrees of freedom of the metric, namely, the radial and latitudinal coordinates, using the Coulomb potential associated with the quasi-Kinnersley transverse frame. These coordinates are invariants of the spacetime and can be used to unambiguously fix the outstanding spin-boost freedom associated with the quasi-Kinnersley frame (and thus can be used to choose a preferred quasi-Kinnersley tetrad). In the limit of small perturbations about a Kerr spacetime, these geometrically motivated coordinates and quasi-Kinnersley tetrad reduce to Boyer-Lindquist coordinates and the Kinnersley tetrad, irrespective of the simulation gauge choice. We explore the properties of this construction both analytically and numerically, and we gain insights regarding the propagation of radiation described by a super-Poynting vector, further motivating the use of this construction in NR simulations. We also quantify in detail the peeling properties of the chosen tetrad and gauge. We argue that these choices are particularly well-suited for a rapidly converging wave-extraction algorithm as the extraction location approaches infinity, and we explore numerically the extent to which this property remains applicable on the interior of a computational domain. Using a number of additional tests, we verify numerically that the prescription behaves as required in the appropriate limits regardless of simulation gauge; these tests could also serve to benchmark other wave extraction methods. We explore the behavior of the geometrically motivated coordinate system in dynamical binary-black-hole NR mergers; while we obtain no unexpected results, we do find that these coordinates turn out to be useful for visualizing NR simulations (for example, for vividly illustrating effects such as the initial burst of spurious *junk* radiation passing through the computational domain). Finally, we carefully scrutinize the head-on collision of two black holes and, for example, the way in which the extracted waveform changes as it moves through the computational domain.

DOI: 10.1103/PhysRevD.86.084020 PACS numbers: 04.25.D−, 04.30.−w, 04.25.dg

I. INTRODUCTION

Numerical relativity (NR) has made great strides in recent years and is now able to explore binary black hole, black-hole—neutron-star, and neutron-star—neutron-star mergers in a wide variety of configurations (see Refs. [1,2] for recent reviews). Numerical simulations are crucial tools for calibrating and validating the large template bank of analytic, phenomenological waveforms which will be used to search for gravitational waves in data from detectors such as the Laser Interferometer Gravitational-Wave Observatory [3,4], Virgo [5] and the Large-Scale Cryogenic Gravitational-Wave Telescope [6]. Numerical simulations also make it possible, for the first time, to explore fully dynamical spacetimes in the strong field region, such as the spacetime of a compact-binary merger.

An important attribute of any analysis performed on numerical simulations is the ability to extract information in a manner independent of the gauge in which one chooses to perform the simulation. In this paper, we suggest one such strategy: using a quasi-Kinnersley tetrad adapted to a choice of coordinates which are computed using the curvature invariants of the spacetime. Most calculations presented in this paper are local, allowing our tetrad and choice of geometrically motivated coordinates (and all quantities derived from them) to be computed in real time during a numerical simulation (i.e., without post-processing). The proposed scheme is also applicable throughout the spacetime, allowing us to study phenomena in both the strongly curved and asymptotic flat regions with the same tools.

In order to extract the 6 physical degrees of freedom of a general Lorentzian metric in four dimensions expressed in terms of a tetrad formulation, 10 degrees of freedom have to be specified [see e.g., Ref. [7]]. Of these 10 degrees of freedom, 6 are associated with the tetrad at a particular point on the spacetime manifold, and 4 originate from the freedom to label that point (the choice of gauge). A common choice of tetrad and the one adopted here is the Newman-Penrose (NP) null tetrad, which consists of two real null vectors denoted $\boldsymbol{l}$ and $\boldsymbol{n}$ as well as a complex conjugate pair of null vectors $\boldsymbol{m}$ and $\bar{\boldsymbol{m}}$. As we demonstrate

explicitly in Sec. II, where we consider the mathematical details in greater depth, the tetrad choice is not unique. The freedom to orient and scale the tetrad is expressed by 6 parameters associated with a general Lorentz transformation between two different null tetrads at a fixed point in the spacetime.

In order to extract physically meaningful quantities and to compare results from different simulations and numerical codes, an explicit prescription for the tetrad choice must be made. Two geometrically motivated prescriptions for orientating the tetrad immediately suggest themselves: choosing i) the principle null frame (PNF) or ii) the transverse frame (TF). (By *frame*, we mean a set of tetrads related by a type III transformation [Sec. II C].) The relationship between these two frames and their properties are discussed in greater detail in Secs. II and III; either one of these two choices immediately removes 4 of the 6 possible tetrad degrees of freedom. The remaining 2 degrees of freedom in the tetrad choice are more subtle (see the discussion in Sec. III C).

The procedure we adopt in this paper is to choose a special transverse tetrad which becomes the Kinnersley tetrad [8] in type-D spacetimes. The properties of these tetrads (known as quasi-Kinnersley tetrads, or QKTs) and their importance for NR have previously been explored in detail [9–14]. Part of the motivation for choosing a QKT is implicit in Chandrasekhar's work on the gravitational perturbations of the Kerr black hole [15]: in this work, he showed that for a given perturbation of the Kerr metric (expressed in terms of the Weyl scalar $\delta\Psi_4$), it is always possible, working to linear order, to find a transverse tetrad and a gauge constructed from the Coulomb potential associated with this tetrad such that the Coulomb potential of the perturbed and background metrics are the same.

We revisit these ideas in Sec. III, where we investigate the properties of the quasi-Kinnersley tetrad choice. We concentrate on the implications of the intrinsic geometrical properties of the tetrad, rather than (as previous works have done) focusing on the tetrad's properties in a perturbative limit. For example, we explore the directions of energy flow using the super-Poynting vector, showing that the choice of a QKT naturally aligns the tetrad with the wave fronts of passing radiation. This observation suggests that, "even in the strong field regime," the QKT is a natural, geometrically motivated tetrad choice for observing the flow of radiation and other spacetime dynamics.

After specializing to the transverse frame, there exists two remaining degrees of tetrad freedom: the freedom of the spin-boost transformations. We fix this remaining tetrad freedom by relying on a straightforward extension of Chandrasekhar's work [15] to the strong field regime. We present the mathematical details in Secs. III D and III E: specifically, we use the Coulomb potential $\hat{\Psi}_2$ on the QKT to introduce a pair of geometrically motivated radial and latitudinal coordinates. Note that $\hat{\Psi}_2$ on the transverse frame is spin-boost independent, that the resulting coordinates can be constructed from the curvature invariants I and J only and that these coordinates reduce to the Boyer-Lindquist radial and latitudinal coordinates for Kerr spacetimes. We then use these geometrically motivated coordinates to fix the spin-boost freedom by ensuring that the projection of the tetrad base vectors onto the gradients of the new coordinates obey the relations found for the Kinnersley tetrad in the Kerr limit.

One application of our chosen QKT and geometrically motivated coordinates is gravitational-wave extraction. For isolated, gravitating systems, gravitational radiation is only strictly defined at future null infinity; this is a consequence of the so-called *peeling property* which governs the behavior of the Weyl curvature scalars as measured on an affinely parametrized outgoing geodesic. With the goal of using our tetrad and gauge prescription as a possible wave extraction method, we work out the implications that this peeling property has for the Weyl curvature scalar expressed on the QKT in Sec. III H. We highlight not only the falloff behavior of the QKT Newman-Penrose quantities but also the behavior of the geometrically constructed radial coordinate. We explore graphically some of the implications of the peeling property for the bunching of principle null directions and argue that the directions associated with QKT are the optimal outgoing directions for ensuring rapid convergence of the computed radiation quantities to the correct asymptotic results.

We implement our geometrically motivated coordinates and QKT numerically within the context of a pseudospectral NR code in Sec. IV, and we present a number of numerical simulations demonstrating the behavior of our coordinates and QKT in Sec. V. First, we carry out, for both nonradiative and radiative spacetimes, a few checks to verify that our scheme works correctly regardless of the choice of gauge in the simulation (Secs. V A and V B, respectively). We confirm that we obtain numerically the correct perturbation-theory results, and we suggest that these tests could be used to benchmark other wave-extraction algorithms.

Finally, we examine the application of the QKT scheme to NR simulations of binary-black-hole collisions in Sec. VI, considering both the wave zone and the strong field regions. We consider a 16 orbit, equal-mass binary-black-hole inspiral and a head-on plunge, merger and ringdown, explicitly illustrating many of the ideas in the theoretical discussions of the previous sections. We then briefly conclude with a discussion of our results and of prospects for the further development of our proposed scheme in Sec. VII.

II. MATHEMATICAL PRELIMINARIES

In this section, we briefly summarize some important properties of Newman-Penrose and orthonormal tetrads (Sec. II A), the Weyl curvature tensor (Sec. II B), the

Lorentz transformations of the Newman-Penrose tetrad (Sec. II C), and the Kinnersley tetrad in Kerr spacetime (Sec. II D). Note that here and throughout this paper, letters from the front part of the Latin alphabet are used for four-dimensional coordinate bases, those from the middle part of the Latin alphabet denote quantities in three-dimensional coordinate bases, while Greek indices are used for tetrad bases. Bold-face fonts denote vectors and tensors.

A. Newman-Penrose and orthonormal tetrads

Two types of tetrad bases are particularly useful for the exploration of generic spacetimes, such as the spacetimes of numerical-relativity simulations of compact-binary mergers: i) the NP tetrad basis $\{e^\alpha_a\} = \{l_a, n_a, m_a, \bar{m}_a\}$, and ii) an orthonormal tetrad $\{E^\alpha_a\} = \{T_a, E^2_a, E^3_a, N_a\}$, which is closely related to the NP tetrad as follows. The quantities $\boldsymbol{E}^2$ and $\boldsymbol{E}^3$ are generally associated with angular variables on a closed 2-surface and are related to the complex null vector $\boldsymbol{m}$ by $E^2_a = \sqrt{2}\Re(m_a)$, $E^3_a = \sqrt{2}\Im(m_a)$. Here, $\Re(\boldsymbol{m})$ and $\Im(\boldsymbol{m})$ denote the real and imaginary parts of $\boldsymbol{m}$, respectively. The timelike vector $\boldsymbol{T}$ and spacelike vector $\boldsymbol{N}$ are related to the null vectors $\boldsymbol{l}$ and $\boldsymbol{n}$ by the transformations

$$l^a = \frac{1}{\sqrt{2}}(T^a + N^a), \qquad n^a = \frac{1}{\sqrt{2}}(T^a - N^a). \tag{2.1}$$

The metric expressed on the orthonormal basis is the Minkowski metric, $\gamma^{\alpha\beta} = \mathrm{diag}\{-1, 1, 1, 1\}$, while on the NP tetrad basis, the metric is

$$\eta^{\alpha\beta} = \begin{pmatrix} 0 & -1 & 0 & 0 \\ -1 & 0 & 0 & 0 \\ 0 & 0 & 0 & 1 \\ 0 & 0 & 1 & 0 \end{pmatrix}. \tag{2.2}$$

On the coordinate basis, the components of the metric are given by

$$g^{ab} = \eta^{\alpha\beta} e^a_\alpha e^b_\beta = -2n^{(a}l^{b)} + 2m^{(a}\bar{m}^{b)}. \tag{2.3}$$

B. Representations of Weyl curvature tensor

One aim of this paper is to uniquely fix the NP tetrad basis to obtain a set of NP scalars from which an unambiguous measure of the Weyl curvature (equal to the Riemann curvature in vacuum) can be read off.

On the NP tetrad, the curvature content of the Weyl tensor can be expressed in terms of five complex scalar functions:

$$\Psi_0 = -C_{abcd} l^a m^b l^c m^d \tag{2.4}$$

$$\Psi_1 = -C_{abcd} l^a n^b l^c m^d \tag{2.5}$$

$$\Psi_2 = -C_{abcd} l^a m^b \bar{m}^c n^d \tag{2.6}$$

$$\Psi_3 = -C_{abcd} l^a n^b \bar{m}^c n^d \tag{2.7}$$

$$\Psi_4 = -C_{abcd} n^a \bar{m}^b n^c \bar{m}^d. \tag{2.8}$$

An equivalent description of the Weyl curvature can be found on the orthonormal frame with associated timelike vector $\boldsymbol{T}$. This is done by defining gravitoelectric $\boldsymbol{\mathcal{E}}$ and gravitomagnetic $\boldsymbol{\mathcal{B}}$ tensors by, respectively, twice contracting $\boldsymbol{T}$ with the Weyl tensor and with its Hodge dual:

$$\mathcal{E}_{ij} = h^a_i h^c_j C_{abcd} T^b T^d, \tag{2.9}$$

$$\mathcal{B}_{ij} = -\frac{1}{2} h_i{}^a h_j{}^c \epsilon_{abef} C^{ef}{}_{cd} T^b T^d. \tag{2.10}$$

Here, $\boldsymbol{h}$ denotes the projection operator onto the local spatial hypersurface orthogonal to $\boldsymbol{T}$. The normalization for the Levi-Civita tensors is such that $\epsilon_{0123} = 1$ and $\epsilon_{123} = 1$ in right-handed orthonormal tetrads and spatial triads, respectively, (see Ref. [16] for a discussion of different conventions in literature). These two tensors can be combined to obtain a complex tensor

$$\mathcal{Q}_{ij} \equiv \mathcal{E}_{ij} + i\mathcal{B}_{ij}. \tag{2.11}$$

The curvature information contained in $\mathcal{Q}$ is exactly the same as that contained in the five NP scalars. Recasting this information in terms of $\mathcal{Q}$ allows us to make use of the fact that the $\boldsymbol{\mathcal{E}}$ and $\boldsymbol{\mathcal{B}}$ tensors describe the tidal acceleration and differential frame-dragging to visualize the curvature of spacetime (see, e.g., Refs. [16–20]).

To make the equivalence between Ψ_0, Ψ_1, Ψ_2, Ψ_3, Ψ_4 and $\mathcal{Q}$ explicit, we note that the components of the complex gravitoelectromagnetic tensor expressed on the spatial triad $\{\boldsymbol{E}^2, \boldsymbol{E}^3, \boldsymbol{N}\}$ are

$$\mathcal{Q} = \begin{bmatrix} \Psi_2 - \frac{\Psi_0+\Psi_4}{2} & i\frac{\Psi_0-\Psi_4}{2} & \Psi_1 - \Psi_3 \\ i\frac{\Psi_0-\Psi_4}{2} & \Psi_2 + \frac{\Psi_0+\Psi_4}{2} & -i(\Psi_1 + \Psi_3) \\ \Psi_1 - \Psi_3 & -i(\Psi_1 + \Psi_3) & -2\Psi_2 \end{bmatrix}. \tag{2.12}$$

Furthermore, $\mathcal{Q}$ is symmetric and trace-free ($\mathcal{Q}^i{}_i = 0$). These results follow from direct substitution of the definition of the orthogonal basis vectors in terms of the NP basis vectors [Eq. (2.1)] and the definition of the NP scalars [Eqs. (2.4), (2.5), (2.6), (2.7), and (2.8)] into the definition of $\mathcal{Q}$ [Eqs. (2.9), (2.10), and (2.11)].

Finally, note that for any spacetime in general relativity, there is a set of 16 scalar functions or Carminati-McLenaghan curvature invariants [21] which can be constructed from polynomial contractions of the Riemann tensor. In vacuum, four of these scalars are nonvanishing and comprise a complete set of invariants. These four scalars can be combined into two complex functions I and J and are independent of tetrad choice. In terms of

the quantities already computed in this section, these curvature invariants can be expressed as

$$\begin{aligned} I &= \frac{1}{2}(\mathcal{E}^k{}_i\mathcal{E}^i{}_k - \mathcal{B}^k{}_i\mathcal{B}^i{}_k) + i(\mathcal{E}^k{}_i\mathcal{B}^i{}_k) \\ &= \Psi_4\Psi_0 - 4\Psi_1\Psi_3 + 3\Psi_2^2 \\ J &= \frac{1}{6}(\mathcal{E}^k{}_i\mathcal{E}^i{}_l\mathcal{E}^l{}_k - 3\mathcal{E}^k{}_i\mathcal{B}^i{}_l\mathcal{B}^l{}_k) \\ &\quad - \frac{i}{6}(\mathcal{B}^k{}_i\mathcal{B}^i{}_l\mathcal{B}^l{}_k - 3\mathcal{E}^k{}_i\mathcal{E}^i{}_l\mathcal{B}^l{}_k) \\ &= \begin{vmatrix} \Psi_4 & \Psi_3 & \Psi_2 \\ \Psi_3 & \Psi_2 & \Psi_1 \\ \Psi_2 & \Psi_1 & \Psi_0 \end{vmatrix}. \end{aligned} \tag{2.13}$$

The invariants I and J play a key role in constructing our geometrically motivated coordinate system (Sec. III).

C. Lorentz transformations

There are six transformations of the NP basis vectors e_a^α which retain the form of the metric given in Eq. (2.2). These are the six Lorentz transformations, which parametrize the six degrees of tetrad freedom [15]. The Lorentz transformations can be decomposed into three types depending on which null vector a particular transformation leaves unchanged:

(i) Type I: ($\boldsymbol{l}$ unchanged)

$$\begin{aligned} &\boldsymbol{l} \to \boldsymbol{l}, \qquad \boldsymbol{n} \to \boldsymbol{n} + \bar{a}\boldsymbol{m} + a\bar{\boldsymbol{m}} + a\bar{a}\boldsymbol{l} \\ &\boldsymbol{m} \to \boldsymbol{m} + a\boldsymbol{l}, \qquad \bar{\boldsymbol{m}} \to \bar{\boldsymbol{m}} + \bar{a}\boldsymbol{l}. \end{aligned} \tag{2.14}$$

(ii) Type II: ($\boldsymbol{n}$ unchanged)

$$\begin{aligned} &\boldsymbol{l} \to \boldsymbol{l} + \bar{b}\boldsymbol{m} + b\bar{\boldsymbol{m}} + b\bar{b}\boldsymbol{n}, \qquad \boldsymbol{n} \to \boldsymbol{n} \\ &\boldsymbol{m} \to \boldsymbol{m} + b\boldsymbol{n}, \qquad \bar{\boldsymbol{m}} \to \bar{\boldsymbol{m}} + \bar{b}\boldsymbol{n}. \end{aligned} \tag{2.15}$$

(iii) Type III: (both $\boldsymbol{l}$ and $\boldsymbol{n}$ unchanged up to rescaling)

$$\begin{aligned} &\boldsymbol{l} \to A^{-1}\boldsymbol{l}, \qquad \boldsymbol{n} \to A\boldsymbol{n} \\ &\boldsymbol{m} \to e^{i\Theta}\boldsymbol{m}, \qquad \bar{\boldsymbol{m}} \to e^{-i\Theta}\bar{\boldsymbol{m}}. \end{aligned} \tag{2.16}$$

Here, the scalars a and b are complex, while A and Θ are real and can be combined into a single complex number $\mathcal{A} = A^{-1}\exp(i\Theta)$. The rescaling of $\boldsymbol{l}$ and $\boldsymbol{n}$ in Eq. (2.16) is called boost freedom, and the phase change of $\boldsymbol{m}$ is called the spin freedom. We will follow the convention of Ref. [10] and call a set of tetrads related by type III transformations a *frame*.

Under the different Lorentz transformations, the NP scalars transform as follows:

(i) Type I:

$$\begin{aligned} &\Psi_0 \to \Psi_0 \qquad \Psi_1 \to \Psi_1 + \bar{a}\Psi_0 \\ &\Psi_2 \to \Psi_2 + 2\bar{a}\Psi_1 + \bar{a}^2\Psi_0 \\ &\Psi_3 \to \Psi_3 + 3\bar{a}\Psi_2 + 3\bar{a}^2\Psi_1 + \bar{a}^3\Psi_0 \\ &\Psi_4 \to \Psi_4 + 4\bar{a}\Psi_3 + 6\bar{a}^2\Psi_2 + 4\bar{a}^3\Psi_1 + \bar{a}^4\Psi_0. \end{aligned} \tag{2.17}$$

(ii) Type II:

$$\begin{aligned} &\Psi_0 \to \Psi_0 + 4b\Psi_1 + 6b^2\Psi_2 + 4b^3\Psi_3 + b^4\Psi_4 \\ &\Psi_1 \to \Psi_1 + 3b\Psi_2 + 3b^2\Psi_3 + b^3\Psi_4 \\ &\Psi_2 \to \Psi_2 + 2b\Psi_3 + b^2\Psi_4 \\ &\Psi_3 \to \Psi_3 + b\Psi_4 \qquad \Psi_4 \to \Psi_4. \end{aligned} \tag{2.18}$$

(iii) Type III:

$$\begin{aligned} &\Psi_0 \to A^{-2}e^{2i\Theta}\Psi_0, \\ &\Psi_1 \to A^{-1}e^{i\Theta}\Psi_1, \\ &\Psi_2 \to \Psi_2 \qquad \Psi_4 \to A^2e^{-2i\Theta}\Psi_4, \\ &\Psi_3 \to Ae^{-i\Theta}\Psi_3. \end{aligned} \tag{2.19}$$

For any algebraically general spacetime, two special frame choices exist: the PNF and the TF. The PNF is characterized by the property that $\Psi_4 = 0 = \Psi_0$; starting from a generic tetrad, a PNF can be constructed by appropriate type-I and type-II Lorentz transformations. The TF is characterized by the property that $\Psi_3 = 0 = \Psi_1$; starting from a PNF, a TF can be constructed by additional type-I and type-II Lorentz transformations.

There are three TFs, but only one contains the Kinnersley tetrad in the Kerr limit [10]. In keeping with earlier literature [9,10], we will call this frame the quasi-Kinnersley frame (QKF) and the particular tetrad we pick out of this frame the quasi-Kinnersley tetrad.

D. The Kerr metric and the Kinnersley tetrad

The no-hair theorems [22,23] lead us to expect all binary-black-hole collisions to ring down to the Kerr spacetime after enough time has elapsed. The limiting Kerr metric in Boyer-Lindquist coordinates $(t, r, \theta, \phi)_{\rm BL}$ can be expressed as:

$$\begin{aligned} ds^2 = &-\left(1 - \frac{2Mr}{\Sigma}\right)dt^2 - \frac{4Mar\sin^2\theta}{\Sigma}dtd\phi + \frac{\Sigma}{\Delta}dr^2 + \Sigma d\theta^2 \\ &+ \frac{\sin^2\theta}{\Sigma}[(r^2 + a^2)^2 - a^2\Delta\sin^2\theta]d\phi^2, \end{aligned} \tag{2.20}$$

where M and a are the mass and spin of the black hole, respectively, and the functions entering the metric are defined by

$$\Sigma = \rho\bar{\rho}, \qquad \rho = r - ia\cos\theta, \\ \Delta = r^2 - 2Mr + a^2. \tag{2.21}$$

For the Kerr spacetime, one tetrad introduced by Kinnersley is particularly conducive for calculation. Among other things, on this tetrad, the perturbation equations in the NP formalism decouple [15,24]; this feature allows the perturbation problem to be reduced to the study of a single complex scalar ($\delta\Psi_4$) which governs the radiation content of the perturbed spacetime. The Kinnersley tetrad expressed on a Boyer-Lindquist coordinate basis is given by

$$l^a = \frac{1}{\Delta}[r^2 + a^2, \Delta, 0, a], \tag{2.22}$$

$$n^a = \frac{1}{2\Sigma}[r^2 + a^2, -\Delta, 0, a], \tag{2.23}$$

$$m^a = \frac{1}{\bar{\rho}\sqrt{2}}[ia\sin(\theta), 0, 1, i\csc(\theta)]. \tag{2.24}$$

On the Kinnersley tetrad, the only nonvanishing NP curvature scalar is

$$\Psi_2 = \frac{M}{\rho^3}. \tag{2.25}$$

In the next section, we explore the behavior of the tetrad and curvature quantities defined in this section in cases where the physical metric is well-understood. So doing, we build up some physical intuition which motivates our QKT choice, which we then apply to more complicated spacetimes, such as those found in numerical simulations.

III. PHYSICAL CONSIDERATIONS FOR CHOOSING A TETRAD

In this section, we introduce several ideas which motivate the choice of tetrad and gauge; we will use these ideas to explore spacetimes produced by numerical-relativity simulations.

For our purposes, we wish to adopt a tetrad and gauge with the following properties (not in order of importance):

(1) The tetrad (gauge) reduces to the Kinnersley tetrad (Boyer-Lindquist coordinates) when the spacetime is a weakly perturbed black hole.
(2) The choice of tetrad and gauge should be independent of the coordinate system, including the slicing specified by the time coordinate, used in the NR simulation.
(3) To facilitate their real-time computation during a NR simulation, all calculation should be local as far as possible.
(4) The prescribed use for all computed quantities should be valid in strong field regions as well as in asymptotic regions of the spacetime.
(5) The choice of tetrad directions should as far as possible be tailored to the physical content of the spacetime. For example, in asymptotic regions, one important direction is that of wave propagation; we seek a tetrad that asymptotically is oriented along this direction.
(6) To facilitate gravitational-wave extrapolation (from the location on the NR simulation's computational domain where the waves are extracted to future null infinity $\mathcal{I}^+$), the falloff with radius of what we identify as the radiation field should match that of an isolated, radiating system; i.e., it should satisfy the expected peeling properties.

We now consider in detail how we may achieve these criteria in the course of constructing our QKT.

This section roughly breaks into three parts:

(1) We start (in Sec. III A) by motivating the use of QKF with a new insight regarding the relationship between its **l** basis vector and the super-Poynting vector, which allows it to satisfy criterion 5. We then review the construction of the QKF in Sec. III B.
(2) Next, we concentrate on fixing the spin-boost freedom to select the QKT out of the QKF. First of all, in Sec. III C, we discuss several methods for fixing this freedom which have appeared in literature. Then, we present our proposal to achieve a global and gauge-independent fixing (in Sec. III E) using a pair of geometrically motivated coordinates defined in Sec. III D. We conclude this part with a brief discussion of issues related to the proposed scheme in Secs. III F and III G.
(3) Finally, we discuss (in Sec. III H) the conformity of the final QKT to criterion 6 and further motivate its use.

A. The TF and wave-propagation direction

The Kinnersley tetrad [Eqs. (2.22), (2.23), and (2.24)] is both a PNF and a TF [25] [cf., Sec. II C]; this implies that the Kerr spacetime is Petrov type D. Generic non-type-D spacetimes do not have this property: for them, no tetrad which is both a PNF and a TF exists, so one must decide which if either of these properties to preserve. Here, we do not want Ψ_4, which plays an important role in the perturbation problem, to vanish; therefore, we choose a tetrad which is a TF [9–13]. In fact, one particular advantage of selecting the TF is its ability to identify the direction of wave propagation in the asymptotic region [cf., criterion 5].

In electromagnetism, a local wave vector which points in the normal direction to the surfaces of constant phase (wave fronts) can be defined. If the medium through which the wave is travelling is isotropic, this direction corresponds to the direction of the waves' energy flow, or the ''wave-propagation direction'', which is determined by the direction of the Poynting vector,

$$\mathcal{P}_i = \epsilon_{ijk} E^j B^k, \tag{3.1}$$

where the vectors E^j and B^k are the electric and magnetic field vectors. In this subsection, we summarize the relationship between the QKT and the gravitational waves' counterpart to Poynting vector.

One approach for constructing a geometrically motivated tetrad follows a suggestion by Szekeres [26], which is to create a gravitational compass out of a number of springs. Such a device is sensitive to the spacetime curvature and can be oriented so that the longitudinal gravitational-wave components vanish; mathematically, this amounts to reorienting the observer's tetrad so that it is a TF, which can be done using type-I and type-II transformations to set $\Psi_1 = 0 = \Psi_3$. We note that Chandrasekhar [15] employed the use of a TF for his program of metric reconstruction from a small perturbation in curvature $\delta\Psi_4$ on a background Kerr metric.

Choosing a TF turns out to orient the tetrad along the direction of energy flow, i.e., along the super-Poynting vector [27,28]

$$\mathcal{P}_i = \epsilon_{ijk} \mathcal{E}^j{}_l \mathcal{B}^{kl}, \tag{3.2}$$

which defines a spatial direction associated with the wave-propagation direction [29]. The super-Poynting vector's components in the orthonormal triad $\{E_i^2, E_i^3, N_i\}$, using the explicit form of gravitoelectromagnetic tensor in Eq. (2.12), are

$$\begin{aligned}
\mathcal{P}_{E^2} &= -P_0(0,1) - 3P_0(1,2) - 3P_0(2,3) - P_0(3,4) \\
\mathcal{P}_{E^3} &= P_1(0,1) + 3P_1(1,2) + 3P_1(2,3) + P_1(3,4) \\
\mathcal{P}_N &= \frac{1}{2}(-|\Psi_0|^2 - 2|\Psi_1|^2 + 2|\Psi_3|^2 + |\Psi_4|^2),
\end{aligned} \tag{3.3}$$

where the functions P_0 and P_1 are defined to be

$$P_0(p,q) \equiv \Re(\Psi_p)\Re(\Psi_q) + \Im(\Psi_p)\Im(\Psi_q) \tag{3.4}$$

$$P_1(p,q) \equiv \Re(\Psi_p)\Im(\Psi_q) - \Re(\Psi_q)\Im(\Psi_p). \tag{3.5}$$

By transforming to a TF, where $\Psi_1 = 0 = \Psi_3$, Eq. (3.3) simplifies significantly, becoming

$$\boldsymbol{\mathcal{P}} = \frac{1}{2}(|\Psi_4|^2 - |\Psi_0|^2)\boldsymbol{N}, \tag{3.6}$$

where its direction corresponds to spatial normal direction $\boldsymbol{N}$ fixed by our choice of TF and Eq. (2.1), which relates $\boldsymbol{N}$ to the NP tetrad vectors $\boldsymbol{l}$ and $\boldsymbol{n}$. By selecting the TF, we have oriented the tetrad according to the flow of energy within the spacetime, achieving criterion 5. We believe this is one of the strongest motivating factors for making the TF choice.

B. Computing the quasi-Kinnersley frame on a given spacelike hypersurface

In this subsection, we review the procedure for constructing the TF which contains the Kinnersley tetrad in the Kerr limit. This, as stated before, is named the quasi-Kinnersley frame. We follow mostly the derivation of Ref. [9].

1. A spatial eigenvector problem for the QKF

Numerical relativity simulations typically split the four-dimensional spacetime to be computed into a set of three-dimensional spatial slices. In the usual 3 + 1 split, the spacetime metric g_{ab} is split into a spatial metric h_{ij}, lapse α, and shift β^i according to

$$g_{ab}dx^a dx^b = -\alpha^2 dt^2 + h_{ij}(dx^i + \beta^i dt)(dx^j + \beta^j dt), \tag{3.7}$$

while the Einstein equations in vacuum split into evolution equations (for advancing from one slice to the next)

$$R_{ij} - \frac{1}{2} g_{ij} R = 0 \tag{3.8}$$

and constraint equations (satisfied on all slices)

$$R_{TT} - \frac{1}{2} g_{TT} R = 0, \tag{3.9}$$

$$R_{Tj} - \frac{1}{2} g_{Tj} R = 0, \tag{3.10}$$

where R_{ab} and R are the Ricci tensor and Ricci scalar of the spacetime, respectively, the component T is in the direction normal to the spatial slice and the components i and j lie within the spatial slice.

As mentioned in Sec. II, for a given spatial slice with future directed unit normal $\boldsymbol{T}$, the curvature can be expressed in terms of the gravitoelectric tensor $\boldsymbol{\mathcal{E}}$ and the gravitomagnetic tensor $\boldsymbol{\mathcal{B}}$ defined in Eqs. (2.9) and (2.10). In terms of the 3 + 1 quantities typically computed in NR codes, provided that the Einstein constraint equations are satisfied, the gravitoelectromagnetic tensors in vacuum can be expressed as

$$\mathcal{E}_{ij} = {}^3R_{ij} + KK_{ij} - K_{ik}K^k_j \quad \mathcal{B}_{ij} = -\epsilon_i{}^{kl} D_k K_{lj} \tag{3.11}$$

where K is the trace of the extrinsic curvature K_{ij}, while ${}^3R_{ij}$ and D_k are the Ricci curvature and connection, respectively, associated with the spatial metric h_{ij}.

Given the gravitoelectric and gravitomagnetic tensors, a powerful tool [16,17] for visualizing the curvature of spacetime is a plot of the *vortex* and *tendex* lines, which are the flow lines of the eigenvectors of the gravitoelectromagnetic tensors $\mathcal{E}_{ij}$ and $\mathcal{B}_{ij}$. The QKF is also related to an eigenvalue problem involving $\mathcal{E}_{ij}$ and $\mathcal{B}_{ij}$, albeit a complex one involving the complex tensor $\mathcal{Q} \equiv \boldsymbol{\mathcal{E}} + i\boldsymbol{\mathcal{B}}$. Specifically, it was shown in Ref. [9] that the QKF can be

constructed from the eigenvector $\tilde{\sigma}^i$ which satisfies the eigenvector equation

$$\mathcal{Q}^{\ i}_{j}\tilde{\sigma}^j = -2\hat{\Psi}_2\tilde{\sigma}^i, \tag{3.12}$$

where the eigenvalue $-2\hat{\Psi}_2$ has the value of $-2\Psi_2$ computed on the QKF. Here and throughout the rest of this paper, we adopt the convention of denoting quantities associated with a QKF (such as the NP tetrad vector $\tilde{\boldsymbol{l}}$) with an overscript tilde and quantities associated with the final tetrad, whose spin-boost degrees of freedom have been uniquely fixed (yielding a preferred QKT), with an overscript hat (e.g., $\hat{\boldsymbol{l}}$). As we will show in greater detail later in the section, the QKF's Coulomb potential $\hat{\Psi}_2$ can be constructed out of the curvature invariants I and J of the spacetime and is invariant under spin-boost transformations; therefore, we denote $\hat{\Psi}_2$ with a hat to indicate it has been fixed to its final value.

2. Selecting the correct eigenvalue

For any symmetric matrix $\mathcal{M}$, the eigenvalues associated with the eigenvector problem $\mathcal{M}^i_j\xi^j = \lambda\xi^i$ obey the characteristic equation $p(\lambda) = 0$ where $p(\lambda) = \det(\mathcal{M} - \lambda\mathcal{I})$ and $\mathcal{I}$ is the identity matrix. For a 3×3 matrix, the characteristic equation becomes

$$p(\lambda) = -\lambda^3 + \lambda^2\mathrm{tr}(\mathcal{M}) + \frac{1}{2}\lambda(\mathrm{tr}(\mathcal{M}^2) - \mathrm{tr}^2(\mathcal{M})) + \det(\mathcal{M}). \tag{3.13}$$

If $\mathcal{M}^i_j = \mathcal{Q}^i_j$, direct calculation using Eqs. (2.12) and (2.13) can verify that $\mathrm{tr}(\mathcal{Q}) = 0$, $\det(\mathcal{Q}) = 2J$ and $\mathrm{tr}(\mathcal{Q}^2) = 2I$, which reduces the characteristic polynomial to

$$p_{\mathcal{Q}}(\lambda) = -\lambda^3 + \lambda I + 2J. \tag{3.14}$$

The solution to this cubic equation can be expressed using the speciality index [30] $\mathcal{S} = 27J^2/I^3$ as

$$\lambda = \frac{3J}{I}\frac{W(\mathcal{S})^{1/3} + W(\mathcal{S})^{-1/3}}{\sqrt{\mathcal{S}}}, \tag{3.15}$$

where $W(\mathcal{S}) \equiv \sqrt{\mathcal{S}} - \sqrt{\mathcal{S}-1}$. There are three solutions[1] corresponding to the three transverse frames, but only one (namely the QKF) contains the Kinnersley tetrad in the Kerr limit [10] (and thus satisfies criterion 1).

We must now select the correct eigenvalue to define the QKF. Only one of the three eigenvalues has an analytic expansion around $\mathcal{S} = 1$ (which holds for all type-D spacetimes, including Kerr [30]). We select this eigenvalue (which we denote λ^0) to define the QKF, and so $-2\hat{\Psi}_2 = \lambda^0$. For reference, the series expansion of λ^0 and also the other two eigenvalues $\lambda^\pm$ around $\mathcal{S} = 1$ is

$$\begin{aligned}\lambda^0 &= -2\hat{\Psi}_2 \sim -\frac{2J}{I}\left[-3 + \frac{4}{3}(\mathcal{S}-1) + \cdots\right],\\ \lambda^\pm &\sim -\frac{2J}{I}\left[\frac{3}{2} \pm i\frac{\sqrt{3}}{2}\sqrt{\mathcal{S}-1} - \frac{2}{3}(\mathcal{S}-1) + \cdots\right].\end{aligned} \tag{3.16}$$

In practice, this selection criterion is equivalent to choosing the eigenvalue with the largest magnitude [10].

3. Constructing the QKF tetrad vectors

We now summarize the necessary results that allow the reconstruction of the QKF from the eigenvector of the matrix $\mathcal{Q}$; for a complete derivation, see Ref. [9]. The eigenvector corresponding to the eigenvalue $-2\hat{\Psi}_2$ can be expressed as

$$\tilde{\sigma}^{\ j} = \tilde{x}^j + i\tilde{y}^j, \tag{3.17}$$

where the real vectors $\tilde{x}^j$ and $\tilde{y}^j$ are orthogonal with respect to the spatial metric h_{ij} and their normalization obeys the condition

$$\|\tilde{\boldsymbol{x}}\|^2 - \|\tilde{\boldsymbol{y}}\|^2 = 1. \tag{3.18}$$

Here and throughout this section, we will use $\|\boldsymbol{v}\|$ and $\boldsymbol{v}\cdot\boldsymbol{w}$ to represent norm and inner product of spatial vectors under h_{ij}. The vectors $\tilde{x}^j$ and $\tilde{y}^j$ can in turn be used to define the vectors

$$\begin{aligned}\tilde{\lambda}^i &= \frac{\tilde{x}^i + \epsilon^{ijk}\tilde{x}_j\tilde{y}_k}{\|\boldsymbol{x}\|^2}, \qquad \tilde{\nu}^i = \frac{-\tilde{x}^i + \epsilon^{ijk}\tilde{x}_j\tilde{y}_k}{\|\boldsymbol{x}\|^2},\\ \tilde{\mu}^i &= \frac{\tilde{\lambda}^i + \tilde{\nu}^i + i\epsilon^{ijk}\tilde{\lambda}_j\tilde{\nu}_k}{1 + \tilde{\boldsymbol{\lambda}}\cdot\tilde{\boldsymbol{\nu}}},\end{aligned} \tag{3.19}$$

where the normalization condition on $\tilde{\boldsymbol{\sigma}}$ [Eq. (3.18)] ensures

$$\|\tilde{\boldsymbol{\lambda}}\| = \|\tilde{\boldsymbol{\nu}}\| = \|\Re(\tilde{\boldsymbol{\mu}})\|^2 - \|\Im(\tilde{\boldsymbol{\mu}})\|^2 = 1. \tag{3.20}$$

The resulting vectors $\tilde{\boldsymbol{\lambda}}$, $\tilde{\boldsymbol{\nu}}$ and $\tilde{\boldsymbol{\mu}}$ turn out to be proportional to the spatial projections of QKF basis vectors $\tilde{\boldsymbol{l}}$, $\tilde{\boldsymbol{n}}$ and $\tilde{\boldsymbol{m}}$, respectively. To see this, let the spatial vectors be expressed in terms of a spatial triad E^a_i which is part of an orthonormal tetrad E^a_α with $E^a_0 = T^a$; then, the full QKF tetrad can be constructed as follows:

$$\begin{aligned}\tilde{l}^a &= \frac{|A|^{-1}}{\sqrt{1 - \tilde{\boldsymbol{\lambda}}\cdot\tilde{\boldsymbol{\nu}}}}(T^a + \tilde{\lambda}^i E^a_i),\\ \tilde{n}^a &= \frac{|A|}{\sqrt{1 - \tilde{\boldsymbol{\lambda}}\cdot\tilde{\boldsymbol{\nu}}}}(T^a + \tilde{\nu}^i E^a_i),\\ \tilde{m}^a &= \frac{e^{i\Theta}}{\sqrt{2}}\frac{\sqrt{1 + \tilde{\boldsymbol{\lambda}}\cdot\tilde{\boldsymbol{\nu}}}}{\sqrt{1 - \tilde{\boldsymbol{\lambda}}\cdot\tilde{\boldsymbol{\nu}}}}(T^a + \tilde{\mu}^i E^a_i).\end{aligned} \tag{3.21}$$

[1]The fraction on the right of Eq. (3.15) has a three-sheeted Riemann surface with branch points of order two at $\mathcal{S} = 0$ and $\mathcal{S} = 1$, as well as a branch point of order three at $\mathcal{S} = \infty$. The three different eigenvalues arise from the values on the three sheets, respectively [9].

Note that the residual spin-boost freedom [cf., Eq. (2.16)] has been made explicit in Eq. (3.21) by means of the parameters A and Θ (which have yet to be determined).

Also note that the equation for $\tilde{\boldsymbol{m}}$ above must be modified if the normal to the spatial slice $\boldsymbol{T}$ lies in the plane spanned by $\tilde{\boldsymbol{l}}$ and $\tilde{\boldsymbol{n}}$, since in this special case, the vectors $\tilde{\boldsymbol{\lambda}}$ and $\tilde{\boldsymbol{\nu}}$ turn out not to be independent of each other (as is true generally) but are instead related by $\tilde{\lambda}^i = -\tilde{\nu}^i$. It is unclear whether such a slicing can be found for any spacetime, but once found, it is closely associated with a TF. In this case, the vector $\tilde{\boldsymbol{\mu}}$ is undefined and $\tilde{\boldsymbol{m}}$ should be constructed from any real unit vector $\tilde{\boldsymbol{r}}$ in the spatial 2-plane orthogonal to $\tilde{\boldsymbol{\lambda}}$ and $\tilde{\boldsymbol{T}}$ according to

$$\tilde{m}^a = \frac{e^{i\Theta}}{\sqrt{2}}(\tilde{r}^i + i\epsilon^{ijk}\tilde{\lambda}_j\tilde{r}_k)E^a_i. \tag{3.22}$$

Because the spatial eigenvector problem (3.12) can be solved pointwise, the construction of the QKF is a local procedure and satisfies criterion 3. Furthermore, the procedure can be applied in the strong field region [cf., criterion 4], although the physical interpretation is only clear if the tetrad can be smoothly extended from there to infinity. By choosing our tetrad to be a QKF, we have used up four of the six possible degrees of tetrad freedom and have uniquely fixed the directions associated with the real null vectors $\tilde{\boldsymbol{l}}$ and $\tilde{\boldsymbol{n}}$. We will address the remaining spin-boost freedom in the next three subsections.

C. The spin-boost tetrad freedom

After electing to work in the QKF, the residual tetrad freedom is restricted to a type-III spin-boost transformation [Eqs. (2.16) and (3.21)]. As seen in Eq. (2.19), the boost transformation affects the magnitude of $\tilde{\Psi}_4$, while the spin transformation modifies the phase of $\tilde{\Psi}_4$.

To gain some insight into what the spin-boost transformations do physically, consider a congruence of observers whose world lines are the integral curves of the $\boldsymbol{T}$ field in Eq. (2.1). For these observers, a spin transformation of the tetrad mixes up the two polarizations of gravitational wave by the induced phase rotation[2]; in practice, this rotation occurs because the observers are rotating the orientation of their coordinates and thus redefining what they consider to be the latitudinal and longitudinal directions. Similarly, the boost transformation in Eq. (2.16) alters the velocity with which these observers move along the direction of wave propagation, causing the gravitational wave they observe to be redshifted or blueshifted.

In order to identify the gravitational wave and curvature content contained in Ψ_4 in an unambiguous manner, we need to provide a prescription for fixing A and Θ throughout the spacetime. Note that $\tilde{\lambda}$ and $\tilde{\nu}$ constructed in Eq. (3.19) are dependent on the choice of slicing; thus, simply setting A and Θ in Eq. (3.21) to particular values does not select a tetrad in a slicing-independent manner. Fixing these parameters but altering the slicing will lead to different tetrads in the same frame (the QKF); thus, when we leave A and Θ undetermined, the frame as a whole which we obtain from Eq. (3.21) is slicing-independent.

One example of fixing the spin-boost freedom in a gauge-independent way often used in mathematical analysis is selecting the so-called canonical transverse tetrad (CTT) [25], which is defined by the condition that

$$\Psi_1 = 0 = \Psi_3 \quad \text{and} \quad \Psi_0 = \Psi_4. \tag{3.23}$$

The CTT has the property that the super-Poynting vector given in Eq. (3.6) has vanishing magnitude; in this tetrad, the observers are comoving with local wave front in the asymptotic region and consequently measure $\|\mathcal{P}\| = 0$. Since no physical observer can travel at the speed of light and comove with the wave front, we require a more physically motivated prescription for fixing the spin-boost freedom.

Several approaches for providing such a physically motivated prescription have been suggested. A common approach is to impose conditions on spin coefficients (such as $\epsilon = 0$ [8]). The Kinnersley tetrad for the Kerr metric has spin coefficients[3] which obey $\kappa = \sigma = \lambda = \nu = \epsilon = 0$. The meaning of some of these coefficients can be gleaned from the equations governing how the tetrad evolves along the $\boldsymbol{l}$ direction, namely [15]

$$l^b l^a_{;b} = 2\Re(\epsilon)l^a - \kappa\bar{m}^a - \bar{\kappa}m^a, \tag{3.24}$$

$$l^b m^a_{;b} = 2i\Im(\epsilon)m^a + \bar{\pi}l^a - \kappa n^a. \tag{3.25}$$

If $\kappa = 0$ for example, the null vector $\boldsymbol{l}$ is tangent to a geodesic, and further, if $\Re(\epsilon) = 0$, this geodesic is affinely parameterized.

Note that choosing $\boldsymbol{l}$ to be geodesic or $\kappa = 0$ is not necessarily consistent with choosing to work in a TF, although these conditions are consistent in the Kerr limit. In a TF, the only freedom available to set the spin coefficients to zero is the spin-boost transformation. Since κ transforms as $\kappa \to A^{-2}e^{i\Theta}\kappa$ under Eq. (2.16), the spin coefficient κ cannot be set to zero. The spin coefficient ϵ, on the other hand, transforms as

$$\epsilon \to A^{-1}\epsilon - \frac{1}{2}A^{-2}l^a\nabla_a A + \frac{i}{2}A^{-1}l^a\nabla_a\Theta, \tag{3.26}$$

and can be made to vanish by suitably chosen A and Θ. Equations (3.24) and (3.25), indicate that the condition $\epsilon = 0$ can be used to fix the scaling of $\boldsymbol{l}$ as well as the

[2]Recall that for plane waves on Minkowski background, we have $\Psi_4 = -\ddot{h}_+ + i\ddot{h}_\times$, where h is the metric perturbation.

[3]For how the spin coefficients (which are complex scalars) are defined in terms of the null tetrad, see, e.g., Eq. (1.286) of Ref. [15].

phase of $\boldsymbol{m}$. Setting $\epsilon = 0$ can therefore be used as a means of fixing the spin-boost freedom, but this choice has the disadvantage that Eq. (3.26) must be solved in order to obtain A and Θ, which can be expensive numerically.

In the following subsections, we present an alternative method of fixing the spin-boost freedom by constructing a coordinate system based on the curvature invariants. Differentials of these new coordinates are then used to set the scale or fix the spin degree of freedom of the final QKT. This method avoids the need to solve differential equations by directly imposing local conditions of the tetrad basis vectors.

D. A geometrically motivated coordinate system

In this paper, we fix the spin-boost freedom by exploiting the curvature invariant $\hat{\Psi}_2$ [identified in Eqs. (3.12) and (3.16) and computed using Eq. (3.15)] to define geometrically motivated and unambiguous radial and latitudinal coordinates. The quantity $\hat{\Psi}_2$ can be interpreted as the Coulomb potential experienced by an observer [26], and all observers in a QKF agree on its value. Our prescription for fixing the spin-boost freedom is to effectively tether our observers to a fixed position with respect to the coordinates associated with the instantaneous background Coulomb potential they experience. By doing this, we choose *stationary* observers which watch gravitational waves pass, in contrast to the CTT observers (Sec. III C) which comove with the waves. In the Kerr limit, our choice amounts to selecting a set of stationary observers associated with the Boyer-Lindquist coordinate system.

To illustrate this idea more fully, note that when we work within the QKF, the complex gravitoelectromagnetic tensor from Eq. (2.12) reduces to

$$\tilde{\mathcal{Q}} = \begin{bmatrix} \hat{\Psi}_2 - (\tilde{\Psi}_0 + \tilde{\Psi}_4)/2 & i(\tilde{\Psi}_0 - \tilde{\Psi}_4)/2 & 0 \\ i(\tilde{\Psi}_0 - \tilde{\Psi}_4)/2 & \hat{\Psi}_2 + (\tilde{\Psi}_0 + \tilde{\Psi}_4)/2 & 0 \\ 0 & 0 & -2\hat{\Psi}_2 \end{bmatrix}, \tag{3.27}$$

making $\tilde{\boldsymbol{N}}$ an eigenvector. Of particular interest is the component

$$\tilde{\mathcal{Q}}_{\tilde{N}\tilde{N}} = -2\hat{\Psi}_2 = \mathcal{E}_{\tilde{N}\tilde{N}} + i\mathcal{B}_{\tilde{N}\tilde{N}}. \tag{3.28}$$

As illustrated in detail in Ref. [17] and particularly in Sec. IV A of Ref. [16], within the context of vortexes and tendexes, $\mathcal{E}_{\tilde{N}\tilde{N}}$ measures tidal acceleration and $\mathcal{B}_{\tilde{N}\tilde{N}}$ the differential frame-dragging experienced by a person whose body is aligned along the radial $\tilde{\boldsymbol{N}}$ eigenvector. The frame dragging induced by the angular momentum of the source implies a latitudinal coordinate, and the radial tidal acceleration implies a radial coordinate. The Coulomb potential $\hat{\Psi}_2$ thus contains information about a pair of geometrically motivated coordinates $\hat{r}$ and $\hat{\theta}$.

To relate the Coulomb potential $\hat{\Psi}_2$ to the geometric coordinates $\hat{r}$ and $\hat{\theta}$ in a meaningful way which reduces to the Boyer-Lindquist coordinates in the Kerr limit (thus satisfying criterion 1), we make use of expressions for the Kerr spacetime [Eqs. (2.25) and (2.21)] to define the coordinates. In other words, we define $\hat{r}$ and $\hat{\theta}$ using the complex equation

$$\hat{\rho} = \hat{r} - i\hat{a}\cos(\hat{\theta}) = \left(\frac{\hat{M}}{\hat{\Psi}_2}\right)^{1/3}, \tag{3.29}$$

where $\hat{M}$ and $\hat{a}$ are real constants which become just the mass and spin of the central black hole in the Kerr limit. A discussion regarding these parameters in dynamical simulations follows in Sec. III F. Recall that the Coulomb potential $\hat{\Psi}_2$ can be constructed directly from the curvature invariants I and J of the spacetime; the construction of the coordinates out of curvature invariants makes them slicing- or gauge-independent, thus satisfy criterion 2.

Figures 1 and 2 explore some properties of $\hat{r}$ and $\hat{\theta}$. The first property is the ability to recover the Boyer-Lindquist radial and latitudinal coordinates from a Kerr spacetime expressed in any slicing. A particular example using Kerr-Schild slicing is shown in Fig. 1, where we plot the contours of $\hat{r}$ and $\hat{\theta}$ under Kerr-Schild spatial coordinates (r, θ, ϕ). The resulting figures show that the coordinate transformations between $(\hat{r}, \hat{\theta})$ and (r, θ) (unlike those for Boyer-Lindquist t and ϕ) do not become singular at the event horizon [cf. criterion 4], which coincides with the contour of

$$\hat{r} = \hat{r}_+ \equiv \hat{M} + \sqrt{\hat{M}^2 - \hat{a}^2} \tag{3.30}$$

as expected. The $(\hat{r}, \hat{\theta})$ coordinate system for a dynamical simulation of two equal-mass, nonspinning black holes during their inspiral phase is shown in Fig. 2. The peanut-shaped features in panel (a) make apparent the fact that the coordinate system is adjusting to the intrinsic geometry of the simulation. The cones of constant angular coordinate $\hat{\theta}$ display a wavy feature when compared to the simulation coordinate θ. This feature and its origin will be discussed in greater detail in Sec. VI A, where we explore the binary simulation in more detail.

E. Fixing the spin-boost degrees of freedom

The previous subsection provides us with an unambiguous and geometrically motivated set of radial and latitudinal coordinates which are valid throughout the spacetime and which are independent of the choice of slicing. Our strategy for fixing the last two degrees of tetrad freedom is to require that the tetrad frames can be associated with observers that are in some sense stationary with respect to our geometrically motivated coordinates while also requiring that the selected tetrad reduces to the Kinnersley tetrad in the type-D limit.

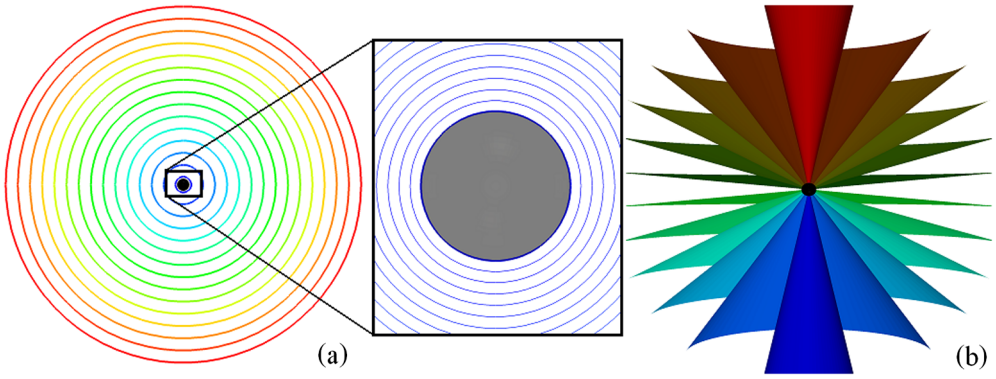

FIG. 1 (color online). Properties of the $(\hat{r}, \hat{\theta})$ coordinates constructed from the Coulomb potential in the QKF. (a) The equatorial plane of a Kerr spacetime in a Kerr-Schild slicing with contours of constant Boyer-Lindquist radius $\hat{r}$ at equal increments. The inset zooms in around the event horizon (indicated by a transparent black disk). The $\hat{r}$ contour increments in the inset, while still uniform, are smaller than in the main figure, and the thick contour line coinciding with the event horizon matches the Boyer-Lindquist radius $\hat{r}_+$ in Eq. (3.30). (b) Surfaces of constant latitudinal coordinate $\hat{\theta}$ for the Kerr-Schild slicing.

To achieve this construction (and thus to provide a global prescription for fixing the spin-boost freedom), note that $d\hat{r}$ provides a measuring rod in the radial direction, relative to the wave front, against which the scale of the radial component of $\hat{\boldsymbol{l}}$ can be fixed. Similarly, $d\hat{\theta}$ provides a transverse direction which can be used to fix the phase of $\hat{\boldsymbol{m}}$. Let us now begin with any tetrad in the QKF $\{\tilde{\boldsymbol{l}}, \tilde{\boldsymbol{n}}, \tilde{\boldsymbol{m}}, \bar{\tilde{\boldsymbol{m}}}\}$, constructed according to Eq. (3.21). The prescription we use to fix the parameters A and Θ associated with the spin-boost degrees of freedom to obtain the final QKT $\{\hat{\boldsymbol{l}}, \hat{\boldsymbol{n}}, \hat{\boldsymbol{m}}, \bar{\hat{\boldsymbol{m}}}\}$ is to require that the final tetrad obeys

$$(d\hat{r})_a \hat{l}^a = 1; \tag{3.31}$$

$$\arg[(d\hat{\theta})_a \hat{m}^a] = \arg[\hat{\rho}]. \tag{3.32}$$

Note that these conditions are exactly the conditions satisfied by the Kinnersley tetrad in Eqs. (2.22) and (2.24) except that the Boyer-Lindquist coordinate has been replaced by its corresponding geometrically constructed counterpart introduced in Sec. III D. The reduction to the Kinnersley tetrad in the type-D limit is thus trivial (cf. criterion 1). Furthermore, conditions (3.31) and (3.32) contain only local differentiation and algebraic calculations and thus obey criterion 3. They also inherit gauge independence from the QKF and the geometric coordinates, thus satisfying criterion 2.

It turns out that the final QKT can be constructed by starting with a tetrad in the QKF with $A = 1$ and $\Theta = 0$ in Eq. (3.21), computing the quantities

$$A = (d\hat{r})_a \tilde{l}^a, \tag{3.33}$$

$$\Theta = -\arg[(d\hat{\theta})_a \tilde{m}^a] + \arg[\hat{\rho}], \tag{3.34}$$

and then substituting these values back into Eq. (3.21) to obtain the final tetrad. Our fictitious observers have now oriented and scaled their tetrads according to the Coulomb potential they experience by observing the local changes in tidal acceleration and differential frame dragging.

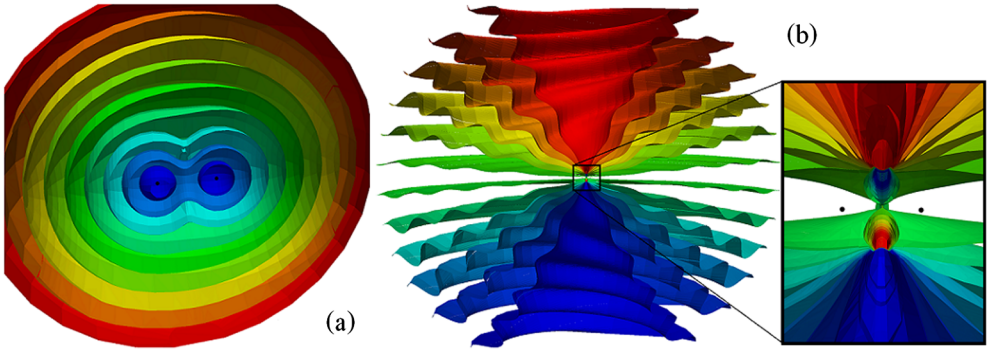

FIG. 2 (color online). (a) Snapshot surfaces of constant $\hat{r}$ for an equal-mass nonspinning binary merger simulation taken during the inspiraling phase. Far away from the black holes, the contours represent those expected from a monopole moment. When moving closer to the black holes, higher-order multipoles become important. (b) Constant $\hat{\theta}$ surfaces for the same simulation as in (a) shows a *spiral-staircase* pattern generated by rotating deformed cones as discussed in greater detail in Sec. VI A.

F. The effect of $\hat{a}$ and $\hat{M}$ on the tetrad choice

In the definition of the geometric coordinates $(\hat{r}, \hat{\theta})$ in Eq. (3.29), two constants $\hat{M}$ and $\hat{a}$ corresponding to the mass and spin of a Kerr black hole in the type-D limit entered our prescription. We now clarify their influence on the final computed quantities of $\hat{\Psi}_4$ and the constructed tetrad.

First, we observe that the spin $\hat{a}$ does not affect the spin parameter Θ in expression (3.34) and can be left undetermined, since only the direction of $d\hat{\theta}$ is required to determine the argument of its inner product with $\tilde{\boldsymbol{m}}$.

The final computed quantities are, however, dependent on the value of $\hat{M}$, which enters as a constant factor scaling the boost parameter A. The computed $\hat{\Psi}_4$ is simply rescaled by a constant scaling factor if the value of $\hat{M}$ is changed. This allows one to compute all quantities real-time during the simulation with (say) $\hat{M} = 1$ and to *a posteriori* rescale the results once the final mass of the remnant black hole is known.

G. The remaining gauge freedom

Using the appropriate combination of the curvature invariants (Sec. III D) to prescribe radial and latitudinal coordinates $(\hat{r}, \hat{\theta})$ fixes two of the four degrees of gauge freedom, while the choice of a TF (Sec. III B) and the subsequent fixing of the spin-boost freedom (Sec. III E) removes all six degrees of tetrad freedom. What remains is to fix the final two degrees of gauge freedom: the slicing (or time coordinate $\hat{t}$) and the azimuthal coordinate $\hat{\phi}$.

For a given slicing, far enough from the strong field region, surfaces of constant $\hat{r}$ and $\hat{\theta}$ intersect in a circle. This can be seen graphically in Fig. 2 by superimposing plot (a) and (b) and taking *far enough* to mean the region where the mass monopole and current dipole are the dominant terms in the Coulomb background. The prescription of the azimuthal coordinate $\hat{\phi}$ is then as simple as requiring that given a specific (as yet undetermined) starting point, the proper distance increments $d\hat{\phi}$ along the circle remains constant.

Fixing the time slicing requires more finesse. One method of specifying the time slicing indirectly is by means of a congruence of outward propagating affinely parameterized null geodesics (see Sec. III H 2 below for a suggested congruence) starting from a fixed radius $\hat{r}$; the affine parameter τ is then used as a coordinate. This approach is particularly suited to the task of wave extraction where the quantities computed should exhibit the scaling laws predicted by the peeling property [31,32].

The prescriptions given above contain residual freedom. Fixing them is beyond the scope of our current work. In this paper, wherever needed, we simply use the coordinate time in the simulation and the simulation's azimuthal coordinate.

H. The peeling theorem

1. Peeling in Newman-Penrose scalars

In this section, we consider the peeling property, which describes the way in which, for an isolated gravitating system which is asymptotically flat, the components of the curvature tensor fall off as one moves farther away from the source of the emitted gravitational radiation. At sufficiently large distances, only type- N radiation is noticeable; the limiting type-N radiation can be identified as the gravitational-wave content of the spacetime (typically denoted as Ψ_4 on an affinely parameterized outgoing geodesic null tetrad). (Note that gravitational radiation is only rigorously defined at future null infinity [denoted $\mathcal{I}^+$]). A caricature of this behavior is given in Fig. 3.

Here, we review the usual derivation of the peeling property [25,31–34], commenting on some of the properties of the QKT within this context; an alternative derivation of the peeling property using spinor notation can be found in Ref. [34].

The basic idea of the usual derivation is to introduce a new *unphysical* metric $d\acute{s}$ which is conformally related to the physical metric ds by $d\acute{s} = \Omega ds$. The metric $d\acute{s}$ is finite and well-defined where the physical metric blows up (points on $\mathcal{I}^+$ are infinitely distant from their neighbors [25]) and allows us to explore the properties of the spacetime at $\mathcal{I}^+$ or at conformal null infinity, where $\Omega \to 0$. All quantities associated with the conformal metric $d\acute{s}$ will be denoted with an acute.

The relationship between metric tensors can be expressed as

$$\acute{g}_{ab} = \Omega^2 g_{ab}, \qquad \acute{g}^{ab} = \Omega^{-2} g^{ab}, \tag{3.35}$$

and the topology at $\mathcal{I}^+$ is $S^2 \times \mathbb{R}$. Now, let l^a be tangent to an affinely parameterized outgoing null geodesic on the real spacetime, with an affine parameter τ such that $l^a \nabla_a \tau = 1$. Then, let $\acute{l}^a$ be tangent to an affinely parameterized geodesic in the conformally related spacetime with affine parameter $\acute{\tau}$. Note that if we take $l^a = \Omega^2 \acute{l}^a$, then the geodesic equation in physical spacetime implies its counterpart in the conformal spacetime [25]; furthermore, if we choose $n^a = \acute{n}^a$ at $\mathcal{I}^+$, then we have that the direction of $(n^a = \acute{n}^a)|_{\mathcal{I}^+}$ does not depend on the geodesic and is tangent to $\mathcal{I}^+$ [25].

Substituting these choices into the expressions for the metric [Eq. (2.3)] and subsequently into Eq. (3.35), we have that at $\mathcal{I}^+$, the conformal tetrad relates to the physical tetrad by means of the expressions

$$l^a = \Omega^2 \acute{l}^a, \qquad m^a = \Omega \acute{m}^a, \qquad n^a = \acute{n}^a. \tag{3.36}$$

Departing from $\mathcal{I}^+$ by moving into the manifold, differences in parallel transport in the physical and conformal manifolds lead to higher-order terms in the $\boldsymbol{m}$ and $\boldsymbol{n}$ equations (see Eqs. (9.7.30) and (9.7.31) in Ref. [25]). By comparing the affine parameter on the two manifolds

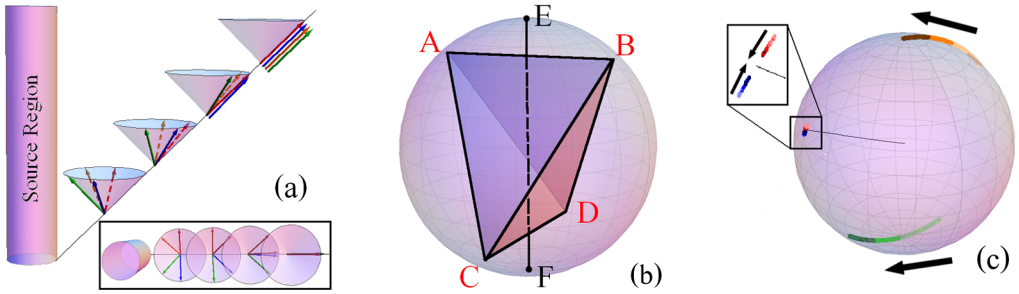

FIG. 3 (color online). (a) A pictorial representation of the peeling property as bunching of PNDs [25], with the inset showing a top-down view. (b) The relationship between the PNDs and the QKT. Points A, B, C and D correspond to PNDs on the anticelestial sphere, and are arranged as the vertexes of a tetrahedron. The anticelestial sphere can be thought of as a spatial slice of the future null cone, where each point on the sphere represents a null direction. The line EF linking the mid-points of a pair of opposite edges strike the anticelestial sphere at opposite poles which correspond to the null direction $\hat{\boldsymbol{l}}$ associated with the QKT at point F and to the null direction $\hat{\boldsymbol{n}}$ associated with the QKT at point E (cf., Fig. 8-5 in Ref. [25]). (c) The four principal null directions recorded during a head-on numerical simulation (described in Sec. IV B) are represented as points (in four different colors) on the anticelestial sphere. We begin integrating a null geodesic in the $\hat{\boldsymbol{l}}$ direction and then compute the PNDs at discrete intervals along that geodesic. Darker-colored points correspond to values farther along the geodesic (farther removed from source region). For cleaner visualization, the angular coordinates on the anticelestial sphere in this figure are simply those of the simulation coordinates and not the abstract ones in Eq. (3.51). We nevertheless see that the PNDs are distributed in a pairwise symmetric manner relative to tangent ℓ of the geodesic (denoted by the black radial line). Two of the PNDs stay close to ℓ, whose close ups are shown in the framed inset. The other two demonstrate a clear motion toward ℓ, where arrows indicate progress along the null geodesic. The numerical findings are thus consistent with the bunching behavior depicted in panel (a).

along a geodesic and imposing Einstein's vacuum field equations, we can show that in general $d\tau = \Omega^{-2} d\acute{\tau}$ and that for large affine parameter τ or small conformal affine parameter $\acute{\tau}$, we have [25]

$$\acute{\tau} = -A^{-2}\tau^{-1} + \sum_{n=2} D_n \tau^{-n}, \tag{3.37}$$

$$\tau = -A^{-2}\acute{\tau}^{-1} + \sum_{n=0} C_n \acute{\tau}^{n}, \tag{3.38}$$

$$\Omega = A^{-1}\tau^{-1} + \sum_{n=2} E_n \tau^{-n}, \tag{3.39}$$

$$\Omega = -A\acute{\tau} - \sum_{n=3} A_n \acute{\tau}^{n}, \tag{3.40}$$

where A_n, C_n, D_n, E_n are constants and $A = -\frac{d\Omega}{d\acute{\tau}}|_{\Omega\to 0}$ is a nonzero constant. Any quantity $\acute{\theta}_{\ldots}$ which is C^h continuous at $\mathcal{I}^+$ can be expressed in terms of a series expansion about $\mathcal{I}^+$ as follows:

$$\acute{\theta}_{\ldots} = \sum_{n=0}^{h} \acute{\tau}^n \acute{\theta}^{(n)}_{\ldots} + o(\acute{\tau}^h) = \sum_{n=0}^{h} \tau^{-n} \theta^{(n)}_{\ldots} + o(\tau^{-h}). \tag{3.41}$$

Since the Weyl tensor is conformally invariant, $C^a{}_{bcd} = \acute{C}^a{}_{bcd}$, or

$$C_{abcd} = \Omega^{-2} \acute{C}_{abcd}, \tag{3.42}$$

all the relevant quantities can be computed on the conformal manifold where the metric is finite and well-behaved, and then interpreted on the physical manifold where the metric quantities may have diverged. At $\mathcal{I}^+$ in an asymptotically flat spacetime, the Weyl tensor $\acute{C}_{abcd}$ vanishes, and the dynamics of the gravitational field as one approaches $\mathcal{I}^+$ can be described using a tensor $\acute{K}_{abcd}$, where

$$\acute{C}_{abcd} = \Omega \acute{K}_{abcd} \tag{3.43}$$

and the components of $\acute{K}$ expressed on the tetrad basis $\{\acute{\boldsymbol{l}}, \acute{\boldsymbol{n}}, \acute{\boldsymbol{m}}, \acute{\bar{\boldsymbol{m}}}\}$ admit expansions in the form of Eq. (3.41).

The peeling-off property of the Weyl scalars naturally arises when one expresses the quantities related to $\acute{\boldsymbol{K}}$ in terms of the physical metric and the tetrad basis $\{\boldsymbol{l}, \boldsymbol{n}, \boldsymbol{m}, \bar{\boldsymbol{m}}\}$. Let us take a detailed look at Ψ_4: analogous to the definition of Ψ_4 in Eq. (2.8), let

$$\acute{\Psi}_4 = -\acute{K}_{abcd} \acute{n}^a \acute{\bar{m}}^b \acute{n}^c \acute{\bar{m}}^d. \tag{3.44}$$

The fact that $\acute{\boldsymbol{K}}$ is regular as we approach $\mathcal{I}^+$ implies that $\acute{\Psi}_4$ admits a series expansion of the form

$$\acute{\Psi}_4 = \sum_{n=0} \tau^{-n} \Psi_4^{(n)}, \tag{3.45}$$

where in particular $\Psi_4^{(0)} = \acute{\Psi}_4|_{\mathcal{I}^+}$. Similar expansions can be found for $\acute{\Psi}_i$, $i = 0, 1, 2, 3$. At $\mathcal{I}^+$, the physical Ψ_4 [defined by Eq. (2.8)] is related to $\acute{\Psi}_4$ by

$$\Psi_4 = -(\Omega^{-2}\acute{C}_{abcd})(\acute{n}^a)(\Omega\acute{\bar{m}}^b)(\acute{n}^c)(\Omega\acute{\bar{m}}^d) = \Omega\acute{\Psi}_4, \tag{3.46}$$

where we have used Eqs. (3.36), (3.42), and (3.43). By a similar argument as used for Ψ_4, the differing powers of Ω appearing in Eq. (3.36) result in a hierarchy being set up where

$$\Psi_i = \Omega^{5-i}\acute{\Psi}_i. \tag{3.47}$$

This expression is merely a product of the series in Eqs. (3.39) and (3.41). Resumming the product of series implies that the physical Weyl scalars along an affinely parameterized outgoing null geodesic can be expressed as

$$\Psi_i = \tau^{i-5}\sum_{n=0}\tau^{-n}\psi_i^{(n)}, \tag{3.48}$$

where $\psi_i^{(n)}$ are constant along the geodesic.

2. Peeling in principal null directions

Note that the peeling property is not a function of which geodesic is chosen (provided that the geodesic strikes $\mathcal{I}^+$ and is affinely parameterized); on the contrary, it is a feature of the spacetime curvature and the distribution of principal null directions (PNDs) as one approaches $\mathcal{I}^+$. This feature is illustrated graphically in Fig. 3(a): as one moves in toward the source from $\mathcal{I}^+$ along a null geodesic, the PNDs *peel off* away from the geodesic direction [34].

Let us now quantify this behavior more precisely. Starting from the $\boldsymbol{l}$ vector associated with the outgoing null geodesic, perform a type-II Lorentz transformation, so from Eqs. (2.15) and (2.18), we have that the four PNDs can be expressed as

$$\boldsymbol{k} = \boldsymbol{l} + \bar{b}\boldsymbol{m} + b\bar{\boldsymbol{m}} + b\bar{b}\boldsymbol{n}, \tag{3.49}$$

where b takes on the values of the four roots of the complex equation

$$\Psi_0 + 4b\Psi_1 + 6b^2\Psi_2 + 4b^3\Psi_3 + b^4\Psi_4 = 0. \tag{3.50}$$

From Eq. (3.49), it becomes apparent that the magnitude of b determines the extent to which the PNDs depart from the null vector $\boldsymbol{l}$ since $k^a l_a = -b\bar{b}$. By making the identification proposed in Ref. [10] between a pair of spherical coordinates (θ, ϕ) and the boost b,

$$b_{(i)} = \cot\left(\frac{\theta_i}{2}\right)e^{i\phi_i}, \qquad i \in \{1, 2, 3, 4\}, \tag{3.51}$$

we can graphically demonstrate the motion of the PNDs by plotting the four roots on the anticelestial sphere as shown in Fig. 3(b). (The anticelestial sphere can be thought of as the space of all possible directions associated with outgoing null rays.) If $\theta_i = \pi$, then the magnitude of the boost $b_{(i)}$ vanishes and $\boldsymbol{k} = \boldsymbol{l}$ is a PND; on the other hand, if $\theta_i = 0$, then $\boldsymbol{k} \propto \boldsymbol{n}$.

Asymptotically, where the Weyl scalars admit power series expansions such as Eq. (3.48), we can obtain the dominant behavior of b by setting

$$b = \sum_{n=0}\tau^{-n}b^{(n)} \tag{3.52}$$

and substituting this expression into Eq. (3.50). We then have that $b^{(0)} = 0$ and $b^{(1)}$ can be found by finding the four roots of the equation

$$\psi_0^{(0)} + 4b^{(1)}\psi_1^{(0)} + 6(b^{(1)})^2\psi_2^{(0)} + 4(b^{(1)})^3\psi_3^{(0)} + (b^{(1)})^4\psi_4^{(0)} = 0. \tag{3.53}$$

Further higher-order terms become more complicated and involve mixtures of higher-order terms in the expansions of the Weyl tensor components.

The leading-order coefficients $\psi_i^{(0)}$ in Eq. (3.48) are independent of the choice of geodesic path, while higher-order terms $\psi_i^{(n)}$ with $n > 0$ are path- or geodesic-dependent, which implies in turn that the $b^{(n+1)}$ are geodesic-dependent. This path dependence suggests the possible existence of an optimal null trajectory along which the series converges most rapidly and from which the gravitational-wave content can be most effectively extracted. One approach to finding the optimal trajectory is to minimize the higher-order terms, $\psi_i^{(n)}$ $(n > 0)$, achieving a rapidly converging series. Possibly the most rigorous method of ensuring rapid convergence would be to identify the Kinnersley tetrad and thus the wave propagation direction at $\mathcal{I}^+$ and then to integrate backward in time, but such a strategy cannot be executed real-time during a numerical simulation.[4] Instead, the method advocated here is to align the initial geodesic direction with the wave-propagation direction in the computational domain and then to integrate forward in time. This direction can be identified in a slicing-independent way by $\hat{\boldsymbol{l}}$ in the QKT as was shown in Sec. III A. In Sec. VI, we will demonstrate numerically the rapid convergence rate which results from this approach.

Choosing the QKT $\hat{\boldsymbol{l}}$ as the initial direction is further justified by considering the manner with which PNDs converge onto the outgoing geodesic's tangent direction. In the QKT, $\hat{\Psi}_1 = 0 = \hat{\Psi}_3$, which greatly reduces the complexity of Eq. (3.50). The transformation from $\hat{\boldsymbol{l}}$ to PND takes the simplified form

$$\hat{b}^2 = \frac{1}{\hat{\Psi}_4}(-3\hat{\Psi}_2 \pm \sqrt{9\hat{\Psi}_2^2 - \hat{\Psi}_4\hat{\Psi}_0}). \tag{3.54}$$

The four roots now occur in pairs and can be parameterized using only two angles.

$$\begin{aligned} \hat{b}_{(1)} &= \cot\left(\frac{\hat{\theta}_1}{2}\right)e^{i\hat{\phi}_1}, & \hat{b}_{(2)} &= \cot\left(\frac{\hat{\theta}_1}{2}\right)e^{i\hat{\phi}_1+i\pi} \\ \hat{b}_{(3)} &= \cot\left(\frac{\hat{\theta}_2}{2}\right)e^{i\hat{\phi}_2}, & \hat{b}_{(4)} &= \cot\left(\frac{\hat{\theta}_2}{2}\right)e^{i\hat{\phi}_2+i\pi}. \end{aligned} \tag{3.55}$$

The outgoing null direction $\hat{\boldsymbol{l}}$ of the QKT thus finds itself in the center of the four PNDs due to the added symmetry imposed by the QKT. This situation is depicted graphically in Fig. 3(b). By initially selecting a QKT direction in the

[4]Note that methods which include $\mathcal{I}^+$ in the computational domain, such as hyperboloidal evolution or characteristic extraction provide alternatives to this approach.

interior of the computational domain from which to shoot the geodesics to infinity, we impose an additional symmetry on the manner in which the PNDs approach the geodesic's tangent initially, hoping that this additional symmetry is maintained as the geodesic approaches $\mathcal{I}^+$ to ensure the clean pairwise convergence of the PNDs to the geodesic's tangent.

Once the geodesic is shot off in the $\hat{\boldsymbol{l}}$ direction, there is nothing to ensure that it remains in the quasi-Kinnersley outgoing null direction. In practice, however, the quasi-Kinnersley property appears to be maintained to a high degree of accuracy, as is indicated by the symmetric pairwise convergence of the PNDs onto the null geodesic shown in Fig. 3(c). For this plot, the angle between the QKT direction of $\hat{\boldsymbol{l}}$ and the tangent ℓ to the geodesic remains less than $4.2 \times 10^{-4}\pi$.

3. Peeling of QKT quantities

We close this section on the peeling property by revisiting the geometrically motivated coordinate system (introduced in Sec. III D) in the asymptotic region. The curvature invariants I and J (and thus $\hat{\Psi}_2$) can be constructed using the series expressions Eq. (3.48). The dominant behavior of the curvature invariants are

$$I \sim \tau^{-6} I^{(0)}, \qquad J \sim \tau^{-9} J^{(0)}, \qquad \hat{\Psi}_2 \sim \tau^{-3} \hat{\psi}_2^{(0)} \tag{3.56}$$

[see Eq. (2.13)] where the quantities with a superscript (0) are constant along the geodesic. Assigning the radial coordinate using Eq. (3.29) sets

$$\hat{r} \sim \tau \Re[(\hat{M}/\hat{\psi}_2^{(0)})^{1/3}]. \tag{3.57}$$

The peeling property states that the PNDs converge onto the outgoing geodesic direction ℓ. Since each pair of PNDs are equidistant from the QKT $\hat{\boldsymbol{l}}$, this implies that $\hat{\boldsymbol{l}}$ approaches the ℓ direction. The asymptotic relationship between $\hat{r}$ and τ given in Eq. (3.57), together with the condition Eq. (3.31) which we use to fix the boost freedom of the QKF, implies that $\hat{\boldsymbol{l}}$ not only asymptotes to the *direction* of ℓ, it is also affinely parameterized in this limit. The geometrically constructed $\hat{r}$ asymptotically denotes the spherical wave fronts of light rays approaching $\mathcal{I}^+$.

Lastly, we underscore the fact that using the QKT has the advantage of identifying a unique affine parameterization of the geodesic as it approaches $\mathcal{I}^+$. The prescription given in Eq. (3.31) for fixing the boost freedom of the QKT has used the geometry of the spacetime implicit in the Coulomb potential to fix the parameterization of $\hat{\boldsymbol{l}}$ in a global manner, removing the freedom to choose a different affine parameter through the transformation $\tau \to A\tau$. These ideas will be revisited in greater detail when we look at extrapolation in the context of the numerical simulations in Sec. IV B.

IV. NUMERICAL IMPLEMENTATION

In this section, we detail the numerical implementation of the analytic ideas mentioned in the previous sections using the SPECTRAL EINSTEIN CODE (SpEC). A description of SpEC and the methods it uses are given in Ref. [35] and the references therein.

A. Constructing the QKT

We construct the QKT in a numerical simulation by first constructing an orthonormal tetrad adapted to the simulation's coordinate choice and then the orthonormal tetrad's null counterpart $\{\boldsymbol{l}, \boldsymbol{n}, \boldsymbol{m}, \bar{\boldsymbol{m}}\}$ and the associated NP scalars Ψ_i. In order to find a QKF $\{\tilde{\boldsymbol{l}}, \tilde{\boldsymbol{n}}, \tilde{\boldsymbol{m}}, \bar{\tilde{\boldsymbol{m}}}\}$, the construction described in Sec. III B can be used; alternatively, the appropriate type-I and type-II transformations [Eqs. (2.14) and (2.15)] to the QKF can be found. Finally, we construct the geometrically motivated coordinate system $(\hat{r}, \hat{\theta})$ described in Sec. III D, and we use these coordinates to fix the remaining type-III tetrad freedom to obtain the QKT.

1. Implementing a coordinate tetrad

Specifically, we begin our construction by noting that the SpEC code stores the spacetime metric g_{ab} on a Cartesian coordinate basis $\{x^a\} = \{t, x, y, z\}$. (Note that, henceforth, the index 0 refers to the time coordinate.) We can also define a set of related spherical coordinates $\{t, r, \theta, \phi\}$ by using the standard definitions

$$x = r\sin\theta\cos\phi, \quad y = r\sin\theta\sin\phi, \quad z = r\cos\theta. \tag{4.1}$$

We further define the timelike unit normal to the spatial slicing and radially outward-pointing vector as

$$T^a = \frac{\delta_0^a - \beta^a}{\alpha}, \qquad N^a = \frac{r^a}{\sqrt{r^b r_b}}, \tag{4.2}$$

respectively, where α is the lapse and β^a is the shift, and $\boldsymbol{r}$ is the spatial location vector. Inserting these orthonormal vectors into Eq. (2.1) yields $\mathbf{l}$ and $\mathbf{n}$, two legs of the null tetrad tied to the simulation's coordinates.

We next construct the remaining two tetrad legs $\{\mathbf{m}, \bar{\mathbf{m}}\}$, ensuring that the normalization conditions of Eq. (2.2) are satisfied. In other words, we seek to construct the null vector $\boldsymbol{m} = 1/\sqrt{2}(\boldsymbol{E}^2 + i\boldsymbol{E}^3)$ where $\boldsymbol{E}^2$ and $\boldsymbol{E}^3$ are orthogonal to $\boldsymbol{T}$ and $\boldsymbol{N}$ and to each other and obey the normalization condition

$$\|\boldsymbol{E}^2\|^2 = \|\boldsymbol{E}^3\|^2 = 1. \tag{4.3}$$

Our construction begins by computing the vectors

$$\boldsymbol{K} = \frac{1}{r\sin\theta}\frac{\partial}{\partial\phi}, \qquad \boldsymbol{F} = \frac{1}{r}\frac{\partial}{\partial\theta}, \tag{4.4}$$

where θ, ϕ are spherical coordinates defined in Eq. (4.1). Then, we ensure orthogonality by means of the Grams-Schmidt-like construction

$$(\hat{F})^a = F^a + F^b l_b n^a + F^b n_b l^a, \tag{4.5}$$

rescaling appropriately to obtain the correct normalization as follows:

$$(E^2)^a = \frac{\hat{F}^a}{\sqrt{\hat{F}^a \hat{F}_a}}. \tag{4.6}$$

Similarly, for the final tetrad leg, we construct the orthogonal vector

$$(\hat{K})^a = K^a + K^b l_b n^a + K^b n_b l^a - K^b E^2_b (E^2)^a, \tag{4.7}$$

normalizing it as follows:

$$(E^3)^a = \frac{\hat{K}^a}{\sqrt{\hat{K}^a \hat{K}_a}}. \tag{4.8}$$

2. Obtaining a tetrad in the QKF

Given the orthonormal coordinate tetrad $\{T^a, (E^2)^a, (E^3)^a, N^a\}$, we next construct a tetrad $\{\tilde{\boldsymbol{l}}, \tilde{\boldsymbol{n}}, \tilde{\boldsymbol{m}}, \bar{\tilde{\boldsymbol{m}}}\}$ in the QKF by using the results of Sec. III B, in particular Eqs. (3.12), (3.17), (3.19), and (3.21). We can alternatively construct a QKF tetrad by explicitly rotating our initial coordinate tetrad into a transverse one via type-I and -II transformations [Eqs. (2.14) and (2.15)]. We have implemented both constructions numerically and verified that they agree; in the remainder of this subsubsection, we discuss details of each implementation in turn.

The hypersurface approach of Sec. III B requires us to solve the complex eigenvector problem in Eq. (3.12), with $\boldsymbol{Q}$ calculated either from Eq. (3.11) or from Eq. (2.12). Using Eq. (2.12), the eigenvector problem can be solved analytically. After computing the desired eigenvalue $\lambda = -2\hat{\Psi}_2$, which is the root of Eq. (3.15) which admits the expansion (3.16) (in practice, it suffices to select the eigenvalue with the largest norm as suggested by Beetle *et al.* [9]), the corresponding un-normalized eigenvector $\tilde{\boldsymbol{\Sigma}}$ of matrix (2.12) is

$$\begin{aligned}
\tilde{\Sigma}_{E^2} &= 2\lambda^2 - \lambda(\Psi_0 + \Psi_4 - 2\Psi_2) \\
&\quad + 2[(\Psi_1 + \Psi_3)^2 - \Psi_2(\Psi_0 + \Psi_4 + 2\Psi_2)], \\
\tilde{\Sigma}_{E^3} &= i[\lambda(\Psi_0 - \Psi_4) + 2(\Psi_3^2 - \Psi_1^2 + \Psi_2(\Psi_0 - \Psi_4))], \\
\tilde{\Sigma}_N &= 2[(\Psi_0 + \Psi_2)\Psi_3 + \lambda(\Psi_1 - \Psi_3) - \Psi_1(\Psi_2 + \Psi_4)],
\end{aligned} \tag{4.9}$$

where the Ψ_i values are those extracted on the coordinate tetrad. (Note that this formula fails when $\Psi_1 = 0 = \Psi_3$, but in this case, the coordinate tetrad is already in the QKF.) To normalize $\tilde{\boldsymbol{\Sigma}}$ into $\tilde{\boldsymbol{\sigma}}$ which satisfies Eq. (3.18), we multiply it with a suitable complex number, namely

$$\tilde{\boldsymbol{\sigma}} = \left[-\frac{1}{\sqrt{2}} \left(\frac{|\alpha|}{\alpha} \right) \frac{\sqrt{\beta + \gamma}}{\gamma} + \frac{\sqrt{2}|\alpha|}{\gamma\sqrt{\beta + \gamma}} i \right] \tilde{\boldsymbol{\Sigma}}, \tag{4.10}$$

where

$$\tilde{\boldsymbol{\Sigma}}^a = \boldsymbol{X}^a + i\boldsymbol{Y}^a, \qquad \alpha = \boldsymbol{X}^a \boldsymbol{Y}_a, \tag{4.11}$$

$$\beta = \|\boldsymbol{X}\|^2 - \|\boldsymbol{Y}\|^2, \qquad \gamma = \sqrt{\beta^2 + 4\alpha^2}. \tag{4.12}$$

Alternatively, we can construct the QKF using the type-I and -II transformations applied to the coordinate frame as follows. Starting from a general Petrov type-I spacetime with five nonvanishing Weyl scalars, we perform a type-I rotation, introducing a parameter $\bar{a}$, followed by a type-II rotation which introduces a parameter b. These parameters can then be chosen to set $\Psi_1 = \Psi_3 = 0$ by solving the resulting system of two equations for the two parameters $\bar{a}$ and b. Reference [10] shows that the appropriate choice of parameters can be found by defining the intermediate quantities

$$H = \Psi_0 \Psi_2 - \Psi_1^2, \qquad G = \Psi_0^2 \Psi_3 - 3\Psi_0 \Psi_1 \Psi_2 + 2\Psi_1^3 \tag{4.13}$$

and then setting

$$\Psi_1 + \Psi_0 \bar{a} = \frac{G \pm \sqrt{G^2 + (\Psi_0 \lambda - 2H)^2 (H + \Psi_0 \lambda)}}{\Psi_0 \lambda - 2H} \tag{4.14}$$

$$b = -\frac{\Psi_3 + 3\bar{a}\Psi_2 + 3\bar{a}^2 \Psi_1 + \bar{a}^3 \Psi_0}{\Psi_4 + 4\bar{a}\Psi_3 + 6\bar{a}^2 \Psi_2 + 4\bar{a}^3 \Psi_1 + \bar{a}^4 \Psi_0}. \tag{4.15}$$

Note that this prescription becomes ill-defined when Ψ_0 on the initial tetrad approaches zero or when $\Psi_0 \lambda - 2H = 0$, making it difficult to find $\bar{a}$ by solving Eq. (4.14); this problem is easily resolved by first applying a type-II transformation which takes the initial tetrad into one in which these pathologies do not arise. Furthermore, we have two possible solutions for $\bar{a}$ resulting from the freedom to interchange the $\tilde{\boldsymbol{l}}$ and $\tilde{\boldsymbol{n}}$ legs associated with the transverse frame; the convention we use is to choose the root which gives $(\tilde{l} - \tilde{n})_a l^a > 0$, i.e., we choose $\tilde{\boldsymbol{l}}$ to be outgoing in the simulation coordinates.

3. Obtaining the quasi-Kinnersley tetrad from the geometric coordinates

With a QKF in hand, we next seek to specialize to the particular QKT described in Sec. III E, where we use geometrically motivated coordinates $(\hat{r}, \hat{\theta})$ given by Eq. (3.29) to fix the final Type III degrees of freedom. In order to fix these freedoms using Eqs. (3.31) and (3.32), we must calculate the one-forms $d\hat{r}$ and $d\hat{\theta}$. We compute the spatial derivatives spectrally, and we compute the time derivatives using the Bianchi identities in the 3 + 1 form [36]

$$\partial_t \mathcal{E}_{ij} = \mathcal{L}_\beta \mathcal{E}_{ij} + \alpha[D_k \mathcal{B}_{l(i}\epsilon_{j)}{}^{kl} - 3\mathcal{E}^k_{(i}K_{j)k} + K^k_k \mathcal{E}_{ij} - \epsilon_i{}^{kl}\mathcal{E}_{km}K_{ln}\epsilon_j{}^{mn} + 2a_k \mathcal{B}_{l(i}\epsilon_{j)}{}^{kl}],$$
$$\partial_t \mathcal{B}_{ij} = \mathcal{L}_\beta \mathcal{B}_{ij} + \alpha[-D_k \mathcal{E}_{l(i}\epsilon_{j)}{}^{kl} - 3\mathcal{B}^k_{(i}K_{j)k} + K^k_k \mathcal{B}_{ij} - \epsilon_i{}^{kl}\mathcal{B}_{km}K_{ln}\epsilon_j{}^{mn} - 2a_k \mathcal{E}_{l(i}\epsilon_{j)}{}^{kl}], \quad (4.16)$$

where $\mathcal{L}$ denotes Lie derivative, D is induced 3D covariant derivative operator, α denotes the lapse, $\boldsymbol{\beta}$ the shift, $\boldsymbol{K}$ the extrinsic curvature and $a_k = \partial_k \ln\alpha$. The time derivative of the metric $\partial_t g_{ij}$ is already known from the numerical evolution of the spacetime. Using the above equations and applying the chain rule, we compute the time derivatives of $\hat{r}$ and $\hat{\theta}$:

$$(\partial_t g_{ij}, \partial_t \mathcal{E}_{ij}, \partial_t \mathcal{B}_{ij}) \overset{\text{Eqs.(2.13),(3.15),(3.29)}}{\longrightarrow} (\partial_t \hat{r}, \partial_t \hat{\theta}).$$

Equipped with all the components of $d\hat{r}$ and $d\hat{\theta}$, we can apply Eqs. (3.33) and (3.34) to fix spin-boost degree of freedom, finally obtaining the QKT on which we can then extract Newman-Penrose scalars $\hat{\Psi}_i$ via Eqs. (2.4), (2.5), (2.6), (2.7), and (2.8).

We note that it may not always be possible to define the $\hat{r}$ and $\hat{\theta}$ coordinates using Eq. (3.29) for spacetimes with additional symmetries. For example, in axisymmetric spacetimes admitting a twist-free azimuthal Killing vector, $\hat{\Psi}_2$ is real, and as a result, the $\hat{\theta}$ coordinate cannot be computed using Eq. (3.29). In fact, for Minkowski spacetimes, we cannot even define the $\hat{r}$ coordinate, because $\hat{\Psi}_2 = 0$. In such cases, the symmetries of the spacetime typically provide a set of preferred coordinates, which one would naturally adopt in a numerical simulation. In our QKT implementation, we presume that any such preferred coordinates are adopted, and we replace $(d\hat{r}, d\hat{\theta})$ by their simulation-coordinate counterparts when degeneracies occur. The majority of astrophysically relevant simulations, however, result in an end state which is spinning such as the Kerr black hole. It should be noted that although this solution is axisymmetric, the azimuthal Killing vector is not twist-free. In this event, the method correctly identifies the Boyer-Lindquist $\hat{r}$ and $\hat{\theta}$ coordinates, and no degeneracies arise.

B. Extrapolation

We now turn to extracting the asymptotic gravitational-wave content at $\mathcal{I}^+$ by using the peeling property, i.e., to *extrapolation*, which necessarily involves information from several spatial slices in the spacetime. Our procedure is to shoot a null geodesic affinely parametrized by τ toward $\mathcal{I}^+$, monitoring $\hat{\Psi}_4$ along the geodesic. The best possible polynomial in $1/\tau$ is fitted to the result. The existence of this polynomial follows from the peeling property, which is made explicit in Eq. (3.48). We identify the coefficient of the $1/\tau$ term or $\psi_4^{(0)}$ with the radiation content at $\mathcal{I}^+$.

In contrast to the usual method (extrapolating Ψ_4 as computed using a tetrad parallel-transported along an outgoing null geodesic), note that here we choose to extrapolate $\hat{\Psi}_4$ (defined using the QKT), which we expect to also display the correct peeling behavior (see Sec. III H 3). In addition, the initial direction of the outgoing null geodesic is along $\hat{\boldsymbol{l}}$, so at the geodesic's starting point $\Psi_4 = \hat{\Psi}_4$, and (Sec. III H), at $\mathcal{I}^+$ also the outgoing null geodesic is along $\hat{\boldsymbol{l}}$ so that $\Psi_4 = \hat{\Psi}_4$. In practice, as we integrate along these outgoing null geodesics, we monitor the difference between the null vector ℓ tangent to the outgoing geodesic and $\hat{\boldsymbol{l}}$ from the QKT, and we find that this difference remains small (cf., Fig. 3 and the surrounding discussion). Therefore ,Ψ_4 and $\hat{\Psi}_4$ are not significantly different for the simulations we examined. When we extract the $\hat{\Psi}_4$ waveform, it converges rapidly to its asymptotic value with increasing extraction radius (Fig. 16).

Selecting the initial tangent of the geodesics to be $\hat{\boldsymbol{l}}$ determines the parameterization of these geodesics up to an additive constant B corresponding to the freedom to shift the zero point of the affine parameter, $\tau \to \tau + B$. The asymptotic waveform is insensitive to the choice of the field B. Nevertheless, to provide an exact prescription, we fix B by recalling that in the Kerr limit, the affine parameter is just the Boyer-Lindquist $\hat{r}$ [15]. We thus choose B on the initial world tube (where we start shooting out null geodesics) to be such that $\tau = \hat{r}$.

C. Sensitivity of QKT method to numerical error

The numerical implementation of the QKT described in this section keeps the computation "as local as possible" in the following sense: the bulk of the calculation requires only local derivatives and knowledge of the metric and the extrinsic and intrinsic curvature of the spatial slice. However, this says nothing about the *accuracy* of our method, which depends on how susceptible our method is to numerical noise.

To begin addressing this issue, we first recall exactly how many numerical derivatives are to be taken. Equation (3.11), which is used to construct the gravitoelectromagnetic tensors $\boldsymbol{\mathcal{E}}$ and $\boldsymbol{\mathcal{B}}$, requires i) second spatial derivatives of the spatial metric in order to get the intrinsic Ricci curvature, in addition to ii) the first spatial derivatives of the extrinsic curvature of the slice. Once the gravitoelectromagnetic tensor is obtained and the resulting curvature invariants I and J are computed, another derivative is required to compute the gradients of the coordinates $(\hat{r}, \hat{\theta})$ which then fix the type-III freedom of the tetrad. Note that the first step, i.e., the computation of the gravitoelectromagnetic tensors, only requires spatial derivatives, which we can compute spectrally (i.e., inexpensively and accurately, since we expect to observe exponential convergence in spatial derivatives with increasing spatial resolution). However, taking the gradient

of the coordinates constructed out of the curvature invariants requires both spatial derivatives and a time derivative. Fortunately, this time derivative can be computed using the Bianchi identities as described in Sec. IV A 3, which again reduces the operation to spatial differentiation (although here the accuracy of the derivatives is also limited by the accuracy at which the constraint equations are satisfied).

What we find in practice is that the higher derivatives needed by our QKT method can at places have a significantly higher amount of numerical noise than the numerical derivatives directly used in the actual evolution system. This is a significant challenge to our method, since SpEC presently evolves the Einstein equations in first-order form, i.e., as a set of coupled partial differential equations containing only first derivatives in space and time. Therefore, the evolution equations themselves will only guarantee the existence of one derivative of the evolution variables (e.g., of the metric). Constraints show convergence which means, among other things, that the auxiliary variables (defined during the reduction of second-order differential equations to first order) do converge to the appropriate metric derivative quantities. However, the evolution system, although quite capable at constraining the size of numerical error, does not necessarily force it to be smooth (differentiable to higher orders) at subdomain boundaries.

Consider the hypothetical example of adding white noise to a smooth analytical metric, such as the Kerr metric (2.20). No matter how small the magnitude of the noise, it would prevent us from taking derivatives analytically. Numerically, under-resolving the high-frequency noise would smooth out the data and allow differentiations to proceed without significantly amplifying the added noise; therefore, we expect that filtering (the spectral equivalent of finite-difference dissipation) would improve the smoothness of the numerical data and thus reduce difficulty in taking higher numerical derivatives. However, such filtering can effectively under-resolve not only noise but also physical information. In other words, overly dissipative schemes tend to be *less* accurate; therefore, the current choice in SpEC is to dissipate as little as possible while still maintaining robust numerical stability. This criterion is different from the use of filtering to damp out on short time scales any high-frequency modes which would be produced during an evolution.

A better approach for reducing nonsmooth numerical error is to go directly to their source. The lack of smoothness in the constraints observed in a typical SpEC evolution is partly due to the penalty algorithm, which is known to produce convergent but nonsmooth numerical errors at subdomain boundaries. [See Fig. 4(b) for an illustration of the penalty-algorithm induced nonsmooth error.] Because this nonsmoothness converges away with increased resolution, our method is observed to be viable given a sufficiently high numerical resolution; however, it remains to be seen whether *sufficiently high* means *significantly higher* than typical resolutions currently in use. Alternatively, improvement to nonsmooth numerical error could come through the use of newer interpatch boundary algorithms, such as discontinuous Galerkin methods [37]. There also exists an ongoing effort to bring a (currently experimental) first-order-in-time, second-order-in-space version of SpEC [38] into a state suitable for accurate gravitational-wave production, with the hope of added efficiency and of achieving numerical error of higher differential order. Such possibilities as these, however, are future work, well outside the scope of this paper.

Lastly, we consider the nonsmooth noise sensitivity of our QKT quantities from another point of view: it can be used as a diagnostic of high-frequency, nonsmooth numerical error. For instance, one source of nonsmooth constraint violation in numerical simulations is the high-frequency, spurious junk radiation present at the beginning of numerical simulations (because of how the initial data are constructed), which poses a particularly difficult numerical problem. The frequency of these modes is of $O(M)$, orders of magnitude higher than that of the orbital motion (and the associated gravitational waves). This makes resolving the junk radiation a difficult task. In the effort to reduce junk radiation, the geometric coordinates can be used as a visualization tool. Fig. 4(a) is an illustration of how the $\hat{\theta}$ contours, plotted as a function of code coordinates, react to the junk travelling through the grid, while adjusting themselves to reflect a more realistic spacetime. By comparing the difference ahead and behind the easily identifiable junk pulse in Fig. 4(a), one gets a glimpse of the missing pieces in the initial data.

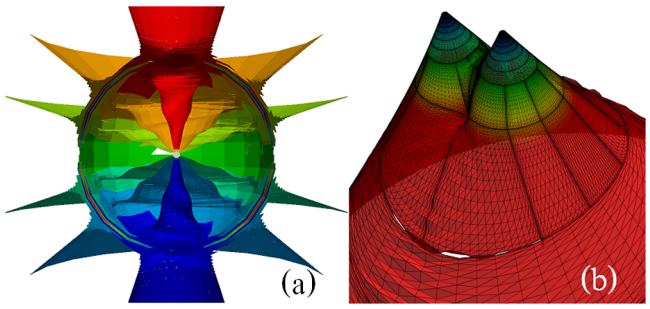

FIG. 4 (color online). (a) $\hat{\theta}$ contours displaying a pulse of high-frequency junk radiation propagating outward. Ahead of the pulse, the geometric coordinate contours are consistent with the Kerr-like initial data, but behind the pulse of junk radiation, the spacetime settles down to an actual binary inspiral with a signature spiral-staircase pattern also seen in Fig. 2(b). (b) The surface is a 2D spatial slice containing the symmetry axis in a head-on simulation, warped and colored according to $\hat{r}$ value. The subdomain boundaries are marked out with dense black lines, and appear to be a source of nonsmooth noise. These noisy features are reduced by increasing resolution.

V. NUMERICAL TESTS OF THE QKT SCHEME

We now consider several numerical tests used to gauge the effectiveness of our proposed QKT scheme for waveform extraction. Most of these tests are motivated by analytic solutions and are used to verify that our choices of geometric coordinates and the QKT are yielding the expected results. These tests broadly fall into two classes: (i) nonradiative spacetime tests and (ii) radiative spacetime tests. Each will be considered in turn in the following subsections.

A. Nonradiative spacetimes

1. Kerr black hole in translated coordinates

The spacetime in this test is a Kerr black hole in Kerr-Schild coordinates, but the coordinate origin is translated away from the black hole along x or z axis. Here, we work in units of the black hole mass, and the dimensionless spin is $J/M^2 = 0.5$ pointing in the z direction. Tetrads determined only by our simulation coordinates [see Eqs. (4.2), (4.3), (4.4), (4.5), (4.6), (4.7), and (4.8)] would not be aware of the translation, and the spatial projection of $\boldsymbol{n}$ would point toward the coordinate center instead of the black hole itself. In contrast, the QKT should adjust to the displaced origin, picking up the true geometrical origin of the gravitating system determined by the Coulomb potential of the QKF. Figure 5 shows the direction of spatial projection of $\boldsymbol{n}$ and $\hat{\boldsymbol{n}}$ associated with the two tetrads. The QKT identifies the black hole at the center of the circular shape, as do the geometrically motivated coordinate $\hat{r}$.

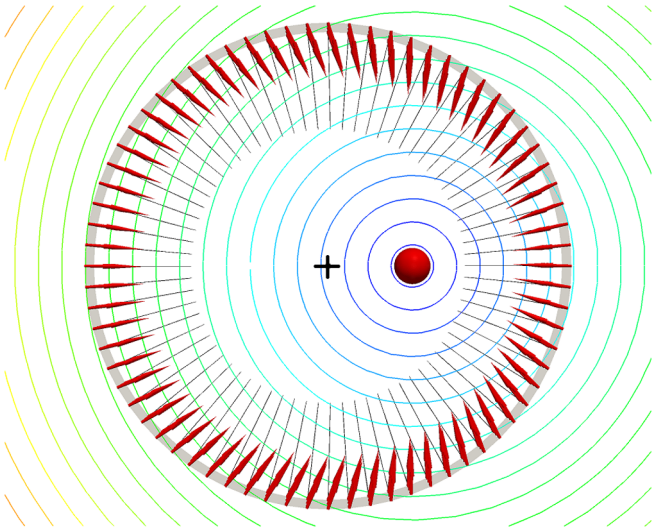

FIG. 5 (color online). A Kerr-Schild black hole with $J/M^2 = 0.5$, with the coordinates translated a distance $9M$ along x axis. The solid (red) sphere indicates location of the black hole's horizon, and the cross (black) indicates the coordinate origin. The concentric circles centered on the solid sphere are constant geometric radius $\hat{r}$ contours; these demonstrate the ability of our geometric coordinates to select an origin based on the Coulomb potential of the QKF, i.e., an origin which reflects the gravitational curvature of the spacetime. Also shown are the spatial projections of the $\boldsymbol{n}$ direction of the coordinate and quasi-Kinnersley tetrads, at points on a narrow strip marked by a ring (gray) centered on the cross. The thin straight lines (black) indicate the $\boldsymbol{n}$ direction associated with the coordinate tetrad, which point toward the coordinate origin, and the thick lines/arrows (red) are QKT $\hat{\boldsymbol{n}}$ directions which identify the black hole as the geometric origin, away from which the gravitational waves travel.

Figure 6 compares Ψ_4 extracted using the coordinate and quasi-Kinnersley tetrads, respectively, using the so-called "L_2 norm" as a measure. The L_2 norm of a quantity X is defined here as

$$L_2(X) = \sqrt{\sum_{i=1}^{N_{\rm tot}} \frac{X(x_i)^2}{N_{\rm tot}}}, \tag{5.1}$$

where x_i are the spectral collocation points of a pseudo-spectral grid and $N_{\rm tot}$ is the total number of points. The present study uses four spherical shells between radii 50 and 140 M with $N_{\rm tot} \approx 4 \times 45^3$ collocation points. The QKT correctly produces vanishing $\hat{\Psi}_4$ (up to numerical roundoff error), while the coordinate tetrad fails to identify the correct outgoing direction and as a result misinterprets $\hat{\Psi}_2$ as gravitational radiation content in Ψ_4. (We observe

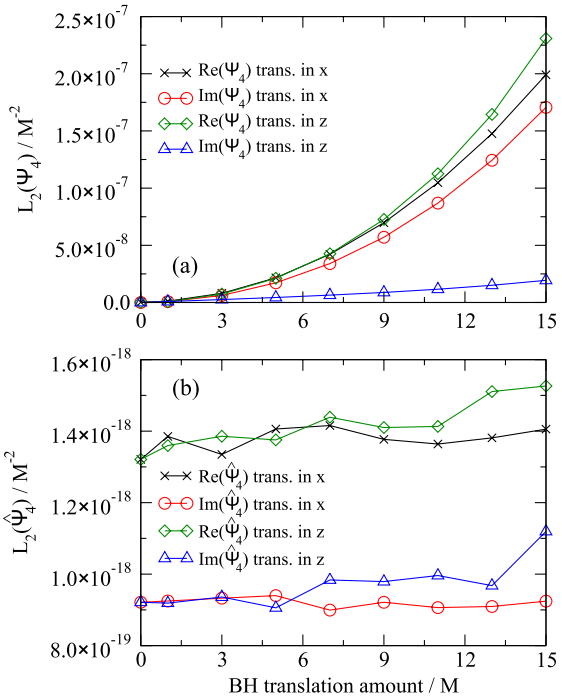

FIG. 6 (color online). (a): The L_2 norm [Eq. (5.1)] of Newman-Penrose scalar Ψ_4 computed (between radii 50 and 140 M) for the Kerr-Schild black hole in translated coordinates on the coordinate tetrad. (b): The Newman-Penrose scalar $\hat{\Psi}_4$ computed in the quasi-Kinnersley tetrad. Note the L_2 norm is eleven orders of magnitudes smaller for the QKT when compared to that of the coordinate tetrad, showing that the QKT correctly adapts to the underlying curvature of the spacetime.

similar behavior for Ψ_0.) Using such a coordinate tetrad in a simulation with a displaced center will result in spurious effects being picked up in the extracted radiation, of a magnitude not necessarily smaller than the physical gravitational-wave content of the spacetime.

In a simulation of a dynamical spacetime, a similar effect should be expected when the "center of mass" (e.g., in a Newtonian approximation) of the system does not coincide with coordinate center. For example, consider a binary merger of unequal mass holes with the coordinate origin placed at the midpoint between the black holes; Ψ_4 extracted at finite radii would pick up a slowly varying offset at an integer multiple of the orbital frequency, and this contribution would complicate the extrapolated waveform.

2. A Schwarzschild black hole with translated coordinates and a gauge wave

We further explore the effects of coordinate choice or gauge by introducing a time-dependent gauge wave into a Schwarzschild solution whose origin has been translated by a constant amount. The resulting metric components now have an explicit time dependence, and we expect the coordinate tetrad to produce a false gravitational wave signal, even though the Schwarzschild spacetime is static and emits no physical radiation.

The exact analytic solution we use for this test is constructed from the Schwarzschild solution in ingoing Eddington-Finkelstein coordinates. We then apply a time-dependent coordinate transformation which yields a metric of the form

$$\begin{aligned} ds^2 = &-(1+C)^2\left(1-\frac{2M}{r}\right)dt^2 \\ &+2(1+C)\left[\frac{2M}{r}-\left(1-\frac{2M}{r}\right)C\right]dtdr \\ &+(1+C)\left[1+\frac{2M}{r}-\left(1-\frac{2M}{r}\right)C\right]dr^2+r^2d\Omega^2, \end{aligned} \tag{5.2}$$

where $C(r,t)$ is the radial waveform of the introduced gauge wave. For our test, we select generically chosen parameters

$$C = 0.7\sin(0.03(t+r)+3.1), \qquad M = 1. \tag{5.3}$$

Note that again we translate the black hole off the coordinate origin by a constant amount (here, $r = 20$M) as described in the previous subsubsection.

Figure 7 shows spin-weighted spherical harmonic expansion coefficients $\Psi_4^{(l,m)}$ of Ψ_4, computed using the coordinate and quasi-Kinnersley tetrads. While only the three largest amplitudes are shown, we have computed all amplitudes up through $l = 35$. These scalars are computed on a sphere at a radius of 120 M from the black hole, with the poles of harmonics aligned with the direction in which the black hole is shifted. As expected, the waveform

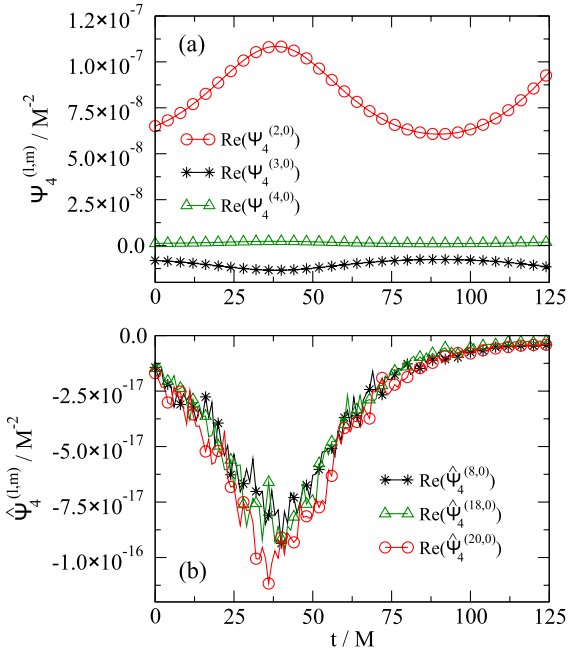

FIG. 7 (color online). Spherical harmonic coefficients of Newman-Penrose Ψ_4 computed for the gauge wave solution, on a sphere of radius $r = 120$M centered on the black hole. (a) Ψ_4 extracted on the coordinate tetrad. (b) $\hat{\Psi}_4$ extracted on the QKT. Only the three largest (l, m) spin-weighted spherical harmonic modes (up through $l = 35$) are shown. Note the scaling on the two figures differ by nine orders of magnitude.

extracted using the coordinate tetrad picks up a time dependence associated with the gauge wave, while the QKT returns vanishing values, correctly identifying the static spacetime solution.

In the generalized harmonic form of the Einstein field equations, the gauge may be set by the covariant wave equations

$$\Box x^a = H^a, \tag{5.4}$$

where H is either a specified or evolved source function [39–42]. It is thus probable that gauge modes similar to the one considered in this example may be present in fully dynamical simulations. Consider a gauge wave which generates a deviation between the coordinate tetrad basis vectors $\{\boldsymbol{l}, \boldsymbol{n}, \boldsymbol{m}, \bar{\boldsymbol{m}}\}$ and their counterparts in the QKT. Such differences can be represented by a sequence of type-II, -I and then -III transformations parametrized by the time-dependent transformation parameters $b(t)$, $a(t)$ and $\mathcal{A}(t)$ which appear in Eqs. (2.15), (2.14), and (2.16), respectively. If we restrict ourselves to asymptotic regions where $\hat{\Psi}_4$ dominates over other NP scalars, then according to Eqs. (2.18), (2.17), and (2.19), we have that to leading order in a and b, the coordinate Ψ_4 is given by

$$\Psi_4 = (1+4\bar{a}(t)b(t))\mathcal{A}^{-2}(t)\hat{\Psi}_4. \tag{5.5}$$

If the gauge wave falls off when we move away from the source region, then we may have

$$(1 + 4\bar{a}(t)b(t))\mathcal{A}^{-2}(t) \to 1, \tag{5.6}$$

and its effect can in principle be extrapolated away. However, for some cases, such as a plane gauge wave, the time-dependent perturbation introduced into Ψ_4 could persist in the extrapolated waveform. Therefore, minimizing any such gauge-dependent content in Ψ_4 extracted at finite radii is preferable to relying on extrapolation to remove them; some pathological gauge modes might not fall off sufficiently quickly with radius.

B. Radiative spacetimes

Having observed that the QKT correctly reflects the curvature content of nonradiative spacetimes, including in the presence of a gauge wave, we next apply the QKT to spacetimes emitting gravitational radiation. In this subsection, we verify that the scheme is consistent with analytic perturbation theory results.

The QKT by construction reduces to the Kinnersley tetrad in the Kerr limit. Therefore, if we perturb a Kerr black hole by a small amount, the $\hat{\Psi}_4$ computed on the QKT should reproduce the analytic perturbation theory results computed on the Kinnersley tetrad associated with the unperturbed Kerr background. Verifying this correspondence provides us with the means to quantitatively test whether the QKT extracts the correct waveform and that we have all normalization conventions implemented correctly. The idea of ensuring the correspondence between the computed waveform and the perturbation theory results is what motivated the authors of Ref. [9] to adopt transverse tetrads in the first place; Chandrasekhar [15] also used the transverse tetrad in his metric reconstruction program, where he explicitly computed the perturbed tetrad and curvature perturbations on the tetrad, obtaining the expected correspondence. For simplicity, here we perturb a Schwarzschild black hole with an odd-parity Regge-Wheeler-Zerilli (RWZ) perturbation, as described in Ref. [43].

We start with a background Schwarzschild metric in Schwarzschild coordinates expressed in the standard form of [43]

$$ds^2 = (-\alpha^2 + \gamma^2\beta^2)dt^2 + 2\gamma^2\beta dt dr + \gamma^2 dr^2 + r^2(d\theta^2 + \sin^2\theta d\phi^2), \tag{5.7}$$

where

$$\alpha(r) = \sqrt{1 - \frac{2M}{r}}, \qquad \beta(r) = 0, \qquad \gamma(r) = \frac{1}{\alpha(r)}. \tag{5.8}$$

We then introduce $l = 2$, $m = \pm 2$ radiative perturbations. The full RWZ formalism giving the explicit calculation of the perturbed metric is expounded concisely in Appendix A of Ref. [43]; it turns out that the construction of the perturbed metric and the associated perturbed curvature quantities (such as Ψ_4) hinges on one function, the RWZ function Z, which obeys the RWZ equation

$$\frac{\partial^2 Z}{\partial t^2} = c_1\frac{\partial^2 Z}{\partial t \partial r} + c_2\frac{\partial^2 Z}{\partial r^2} + c_3\frac{\partial Z}{\partial t} + c_4\frac{\partial Z}{\partial r} - \alpha^2 V Z. \tag{5.9}$$

In the RWZ equation, the coefficients c_i are functions of α, β and γ, which for our chosen values [Eq. (5.8)] become

$$c_1(r) = 0 = c_3(r), \tag{5.10}$$

$$c_2(r) = \left(1 - \frac{2M}{r}\right)^2, \tag{5.11}$$

$$c_4(r) = \frac{2M}{r^2}\left(1 - \frac{2M}{r}\right), \tag{5.12}$$

$$\alpha^2 V = \left(1 - \frac{2M}{r}\right)\left(l(l+1) - \frac{6M}{r}\right)\frac{1}{r^2}. \tag{5.13}$$

Note that in the discussion which follows, $\underline{\Psi}_4$ denotes the analytic result while Ψ_4 and $\hat{\Psi}_4$ are, respectively, the computed values on the coordinate and quasi-Kinnersley tetrads in the numerical implementation. Given Z, the analytic solution $\underline{\Psi}_4$ for the gravitational-wave content in the spacetime can be computed to first order using

$$\underline{\Psi}_4^{(1)} = -\sum_{lm}\left[\frac{i}{r}(\tilde{\Delta} + 2\gamma + 2\mu)\tilde{\Delta} Z_{lm}\right] C_l[{}_{-2}Y^{lm}], \tag{5.14}$$

where $C_l = \sqrt{(l-1)l(l+1)(l+2)/4}$, the operator $\tilde{\Delta}$ is $\underline{n}^a\nabla_a$ with $\underline{\boldsymbol{n}}$ being a null direction associated with the background Kinnersley tetrad, and γ and μ are spin coefficients associated with the same background tetrad, which for our case are [15]

$$\mu = -\frac{\Delta}{2\Sigma\rho}, \qquad \gamma = \mu + \frac{r - M}{2\Sigma}, \tag{5.15}$$

where Δ, Σ and ρ are defined in Eq. (2.21).

In order to solve the linear second-order partial differential equation (5.9) for Z, an initial value and time derivative for Z must be specified. For our investigation, we make use of a traveling-wave perturbation of the form

$$Z(t_0, r) = A_c e^{i\omega(t_0 - r_*)}, \qquad \frac{\partial Z}{\partial t}(t_0, r) = i\omega A_c e^{i\omega(t_0 - r_*)}, \tag{5.16}$$

where r_* is the usual tortoise coordinate defined by $dr_*/dr = r/(r - 2M)$, while $t_0 = 0$, $\omega = 0.1$ and A_c is a constant initial amplitude. For our test, we also set $M = 1$. This perturbation is graphically depicted in Fig. 8, plotted as surfaces warped according to the $\Re(\Psi_4)$ value as a function of the background Schwarzschild coordinates. The waveform constructed from the perturbation has the classical profile for Ψ_4, often observed during numerical binary black hole mergers; this is to be expected, since

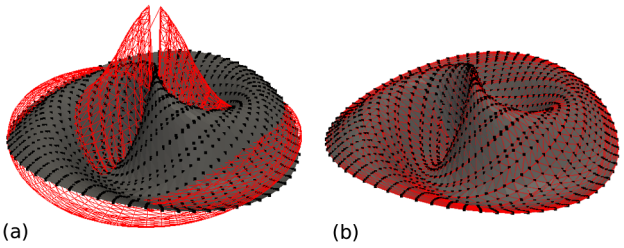

FIG. 8 (color online). $\Re(\Psi_4)$ resulting from a traveling-wave perturbation on the equatorial plane of the computational domain. Panels (a) and (b) correspond to results obtained with and without the coordinate transformation (5.20), plotted with respect to the background Schwarzschild coordinates. We use $\underline{\Psi}_4$, Ψ_4 and $\hat{\Psi}_4$ to respectively denote the analytical result and the values computed on the coordinate and quasi-Kinnersley tetrads. The height of the surface in the vertical direction indicates the value of $\Re(\Psi_4)$, the solid grey surface denotes $\Re(\underline{\Psi}_4)$, the red wire frame $\Re(\Psi_4)$ and the black dots $\Re(\hat{\Psi}_4)$. The amplitude of the red wire frame has been suppressed by a factor of 10^3 in (a) so that it fits into the figure. The suppression factor has not been applied to panel (b).

$l = 2$ is the dominant mode contributing to the gravitational radiation emitted by a binary.

Next, we numerically compare the coordinate-tetrad Ψ_4 and the QKT $\hat{\Psi}_4$ with the analytic perturbation-theory result $\underline{\Psi}_4$. In this test, we adopt the Boyer-Lindquist coordinates; therefore, the corresponding coordinate orthonormal tetrad [see Eq. (4.2)] happens to coincide with a Kinnersley frame of the background spacetime [although it is boosted with respect to the Kinnersley tetrad in Eqs. (2.22), (2.23), and (2.24)].

To illustrate this more clearly, observe that the standard coordinate tetrad we constructed in Sec. IVA 1 results in orthonormal vectors T^a and N^a which are, respectively,

$$T^a = \left[\frac{1}{\alpha}, 0, 0, 0\right], \qquad N^a = [0, \alpha, 0, 0], \tag{5.17}$$

when expressed on the coordinate basis, where $\alpha = \sqrt{1 - 2M/r}$ is the lapse of the background metric. The resulting null vector l^a constructed according to Eq. (2.1) is

$$l^a = \frac{1}{\sqrt{2}}(T^a + N^a) = \frac{1}{\sqrt{2}}\left[\frac{1}{\alpha}, \alpha, 0, 0\right]. \tag{5.18}$$

In the static limit, the Kinnersley tetrad [Eqs. (2.22) and (2.23)] reduces to

$$\hat{l}^a = \left[\frac{1}{\alpha^2}, 1, 0, 0\right], \qquad \hat{n}^a = \frac{1}{2}[1, -\alpha^2, 0, 0], \tag{5.19}$$

so $\hat{l}^a = \sqrt{2} l^a/\alpha$, and there exists a relative boost factor of $A = \alpha/\sqrt{2}$ between the coordinate and Kinnersley tetrads.

Therefore, to account for the difference, we will multiply the coordinate-tetrad Ψ_4 by $(1 - 2M/r)/2$ throughout this subsection to facilitate comparison with analytical and QKT values. With this adjustment, the extracted quantities Ψ_4 and $\hat{\Psi}_4$ both match the analytically calculated $\underline{\Psi}_4$ from perturbation theory. These results are graphically depicted in Fig. 8(b).

Next, we explore the gauge dependence of the QKT result. To this end, we introduce a coordinate transformation into some other gauge. As a result, the coordinate tetrad associated with the new *nonprivileged gauge* differs from the QKT, resulting in a mismatch between the coordinate Ψ_4 and the analytic perturbation theory result $\underline{\Psi}_4$ [see Fig. 8(a)]. The QKT $\hat{\Psi}_4$ implemented in the code should then be able to recover the analytic result. As an illustrative example, for a gauge transformation, we choose a cubic rescaling of the spatial coordinates, which takes the radial vector r^a expressed on a Cartesian coordinate basis defined in Sec. IVA to a vector with components $\tilde{r}^a$ using the equation

$$\tilde{r}^a = \left(\nu + \frac{\nu^0 - \nu}{R^2}|r - r_0|^2\right)(r^a - r_0^a) + r_0^a, \tag{5.20}$$

where we choose $r_0^a = (5\ \mathrm{M}, 0, 0)$, $R = 100\ \mathrm{M}$, $\nu_0 = 1$ and $\nu = 1.1$. Panel (b) of Fig. 9 compares the coordinates before and after rescaling.

We now calculate the perturbed metric in the new distorted coordinates and extract the gravitational waves using both the coordinate tetrad and the QKT, comparing the results with the analytical $\underline{\Psi}_4$ calculated in the Boyer-Lindquist coordinates and visually portrayed in Fig. 8. When no coordinate distortions have been introduced [Fig. 8(b)], the coordinate tetrad and the QKT both generate Ψ_4 which matches the analytical prediction. When we apply the cubic coordinate distortion described above, however, the coordinate tetrad result deviates from $\underline{\Psi}_4$, but the QKT still recovers the analytical value [Fig. 8(a)].

In addition to the coordinate transformation, we also add a $l = 1$, $m = 0$ mode (explicit expressions for metric perturbation due to this mode can be found in Appendix A1a of Ref. [43]). This mode should make no contribution to the detected radiation in $\hat{\Psi}_4$, but should introduce a small angular momentum perturbation affecting the spin of the spacetime, thus avoiding degeneracy in $\hat{\theta}$. The amplitude of the perturbation is usually set so that the spin of the resulting spacetime is $a = J/M = 0.001$. After imposing the coordinate distortion and adding the $l = 1$ $m = 0$ mode, we extract ${}_{-2}Y_{lm}$ coefficients of Ψ_4 and $\hat{\Psi}_4$ on a sphere of Boyer-Lindquist radius 95 M from the black hole. We begin by exploring the effect of the $l = 1$, $m = 0$ mode. Figure 9(a) shows the effect of increasing the strength of the $l = 1$, $m = 0$ perturbation on the $l = 2$, $m = 0$ mode of extracted waveform; recall that we did not introduce an $l = 2$, $m = 0$ mode into the metric perturbation. The coordinate quantity $\Psi_4^{(2,0)}$ shows a constant value possibly originating from the cubic coordinate distortion. The quantity $\hat{\Psi}_4^{(2,0)}$, on the other hand, shows a

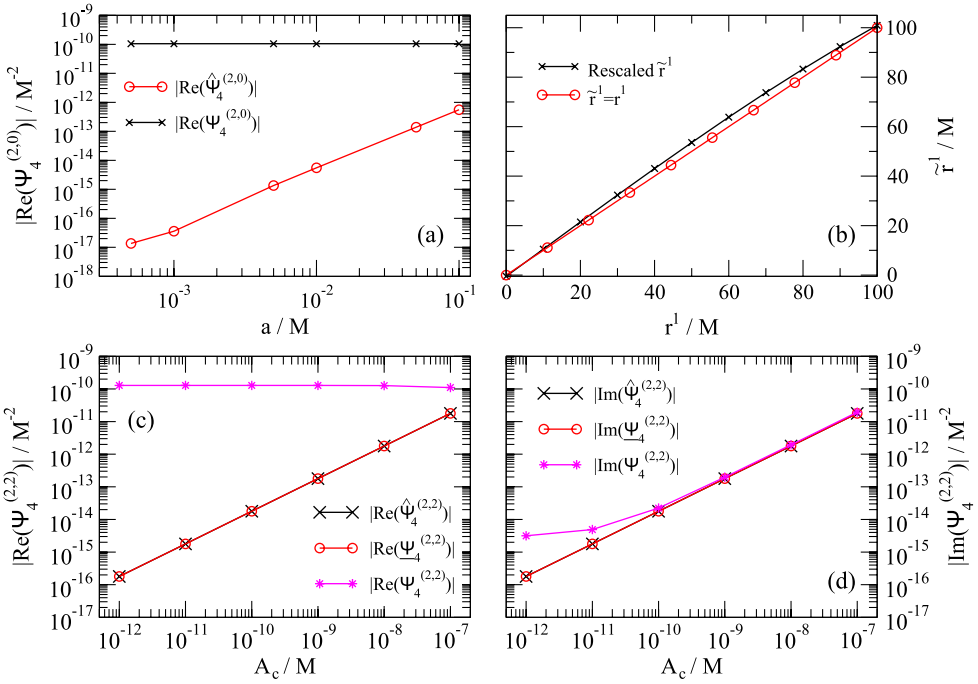

FIG. 9 (color online). Testing the QKT's ability to recover perturbation theory results. An $l = 2$, $m = \pm 2$ perturbation, with magnitude A_c, is added as a function of retarded time in addition to an $l = 1$, $m = 0$ perturbation, and finally a cubic coordinate distortion is applied as described in Eq. (5.20). The spherical harmonic coefficients of the coordinate-tetrad Ψ_4 and QKT $\hat{\Psi}_4$ are then extracted at Boyer-Lindquist radius 95 M and compared with the analytic results $\underline{\Psi}_4$. (a): The magnitude of the Ψ_4, $(l, m) = (2, 0)$ mode as a function of spin parameter a, with the radiative $(2, \pm 2)$ perturbation held fixed at $A_c = 10^{-9}$M. (b): Exploring the effect of cubic rescaling. The rescaled first component of $\tilde{\boldsymbol{r}}$ vector, $\tilde{r}^1$, is plotted against the original component r^1. The identity map ($\tilde{r}^1 = r^1$) is given for comparison. (c) and (d): The real and imaginary parts of the ${}_{-2}Y_{22}$ coefficient vs the amplitude A_c of the radiative perturbation. The $l = 1$, $m = 0$ mode amplitude is chosen so that the resulting angular momentum perturbation is held constant at $a = 0.001$M.

strong dependence on the $l = 1$ perturbation amplitude; this could be due to the fact that the projection onto spherical harmonics, as opposed to spheroidal harmonics, is no longer correct when the perturbing spin is introduced. The effect is, however, small when compared to the magnitude of the $l = 2$, $m = 2$ modes.

The lower panels of Fig. 9 explore the effect of increasing the $l = 2$, $m = \pm 2$ perturbation amplitude A_c on the extracted $l = 2$, $m = \pm 2$ modes. In general, the QKT shows very good agreement with analytical result over a range of perturbation magnitudes as desired, while the quantities computed on the coordinate tetrad disagree significantly with the analytic perturbative result.

VI. APPLICATION OF THE QKT TO NUMERICAL SIMULATIONS OF BINARY BLACK HOLES

We now turn to exploring the properties and effectiveness of the QKT scheme when applied to more generic numerical simulations involving the collision of two black holes. We consider two examples: a circular inspiral of two equal-mass, nonspinning black holes (Sec. VI A) and the head-on collision of two nonspinning, equal-mass black holes (Sec. VI B).

A. Equal-mass, nonspinning binary-black-hole inspiral

In this subsection, we apply our QKT method to a fully dynamical simulation of two equal-mass, nonspinning black holes which inspiral through 16 orbits, merge and ring down. We summarize some of the physical parameters of this simulation in Table I (which is a reproduction of Table II of Ref. [44]); further details of this simulation and the numerical method used are given in Ref. [44] and the references therein.

We examine two aspects of the QKT which we have considered in previous sections: (i) that the direction $\hat{\boldsymbol{l}}$ identified by the QKT corresponds to the wave-propagation direction (as discussed in Sec. III A) and the

TABLE I. Physical properties of the equal-mass, nonspinning binary-black-hole inspiral reported in Ref. [44]. Here, M is the sum of the Christodoulou masses of the initial holes, and M_f is the Christodoulou mass of the final hole.

Initial orbital eccentricity	$e \sim 5 \times 10^{-5}$
Initial spin of each hole	$S_i/M^2 \leq 10^{-7}$
Duration of evolution	$\Delta T/M = 4330$
Final black hole mass	$M_f/M = 0.95162 \pm 0.00002$
Final spin	$S_f/M_f^2 = 0.68646 \pm 0.00004$

implications this has for the geometric coordinates $\hat{r}$ and $\hat{\theta}$, and (ii) that the falloff rates of the Newman-Penrose scalars are consistent with the peeling property (as described in Sec. III H).

1. Wave-propagation direction

If (as claimed in Sec. III A) the vector $\hat{l}$ associated with the QKT correctly identifies the outgoing wave-propagation direction, one would expect that as one follows the wavefront out to infinity, the spacetime curvature along this trajectory and the associated derived quantities should become quite simple. To illustrate this, we consider an S^2 coordinate sphere in the original Cauchy slice and identify the correct null direction $\hat{l}$ associated with the QKT at each point. We then integrate the null geodesic equations outward to produce a null hypersurface and consider this null hypersurface to be a new slicing and a preferred characteristic surface (PCS) of the spacetime. Identifying the geometrical coordinates $\hat{r}$ and $\hat{\theta}$ within this slicing, we plot their contours in the left-hand panels [plots (a) and (c), respectively] of Fig. 10. For comparison, we also show $\hat{r}$ and $\hat{\theta}$ computed within the original Cauchy slice. Note the simplicity of the computed geometric quantities within the PCS associated with the outgoing wave front as opposed to the corresponding quantities computed within the Cauchy surface.

The structure observed within the Cauchy surface can be understood as follows. The holes generate a rotating mass quadrupole approximately given by the Newtonian relation

$$\mathcal{I}_{ij}(t,r) \approx M q^i(t-r) q^j(t-r) - \frac{MR^2}{12}\delta_{ij} = \frac{MR^2}{24}\begin{pmatrix} 3\cos[2\Omega t'] + 1 & 3\sin[2\Omega t'] & 0 \\ 3\sin[2\Omega t'] & -3\cos[2\Omega t'] + 1 & 0 \\ 0 & 0 & -2 \end{pmatrix}, \tag{6.1}$$

where M is total mass of the binary, R is the separation between the two black holes, $\boldsymbol{q}$ is the location of one of the black holes and the choice of coordinates is such that the other black hole is located at $-\boldsymbol{q}$. In the matrix, $\Omega = \sqrt{M/R^3}$ is the orbital angular velocity and $t' = t - r$. This quadrupole moment deforms the $\hat{r}$ contour into an ellipsoid (or peanut shape when closer to the two holes [see Fig. 2(a)]), while its time dependence causes the orientation of the ellipsoid to rotate at a frequency of 2Ω.

On the PCS, the structure is much simpler. The inner contour sets the basic shape for constant $\hat{r}$ surfaces, which are roughly ellipsoidal. These surfaces then expand, retaining their orientation as the distortion is propagated outward at the speed of light along the wave front. Figure 10(a) shows a concentric pattern of $\hat{r}$ contours on the null hypersurfaces, in contrast to the rotating contours on a spatial Cauchy hypersurface which slices through many PCSs, as depicted in Fig. 10(b). The angular $\hat{\theta}$ coordinates similarly display a relative simplicity on the PCS, taking on the shape of a slightly deformed (squashed sideways) cone. Figures 10(c) and 10(d) show the $\hat{\theta}$ surfaces on a PCS and in a spatial slicing, respectively; the orientation of the deformed constant $\hat{\theta}$ cones is independent of the distance to black hole in the PCS, but rotates around when moving outwards on the spatial slice, forming a spiral-staircase pattern.

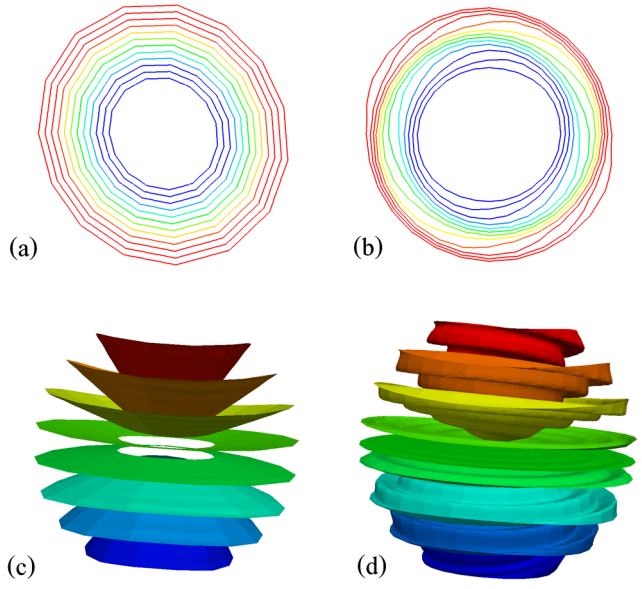

FIG. 10 (color online). Geometrical coordinates obtained from the QKF $\hat{\Psi}_2$. (a) Contours of $\hat{r}$ on a slice of the null preferred characteristic surface generated by the geodesic developments of $\hat{l}$. (b) Contours of $\hat{r}$ on a constant-simulation-time Cauchy slice. (c) Contours of $\hat{\theta}$ on the same null surface as (a). (d) $\hat{\theta}$ contours in the same Cauchy slice as (b).

2. Peeling property

Next, we explore the falloff rate of the Newman-Penrose scalars computed on the QKT as one moves outward along the PCS generators (i.e., along the null geodesics tangent to the QKT $\hat{l}$ where they originate). This rate allows us to quantify to what extent the QKT obeys the peeling property derived in Sec. III H and to what extent the computed quantities are suitable for use in the extrapolation procedure prescribed in Sec. IV B.

To this end, we start with 3510 null geodesics from the grid points of a mesh (of 351 points) covering a sphere of radius $\hat{r} \approx 150\,\mathrm{M}$ surrounding the source region. Over a small time interval of 10 M, a new set of geodesics are shot off every 1 M. The affine parameter τ is initially set to $\hat{r}$, and the geodesics are evolved for around 150 M. The Newman-Penrose $\hat{\Psi}_i$'s are recorded at intervals of $\Delta\tau = 1\,\mathrm{M}$ along the geodesics. A histogram of the best fits for the power-law falloff (i.e., of the slopes of the $\ln(|\hat{\Psi}_i|)$ vs $\ln(\tau)$ graphs) for the 3510 geodesics are plotted in Fig. 11.

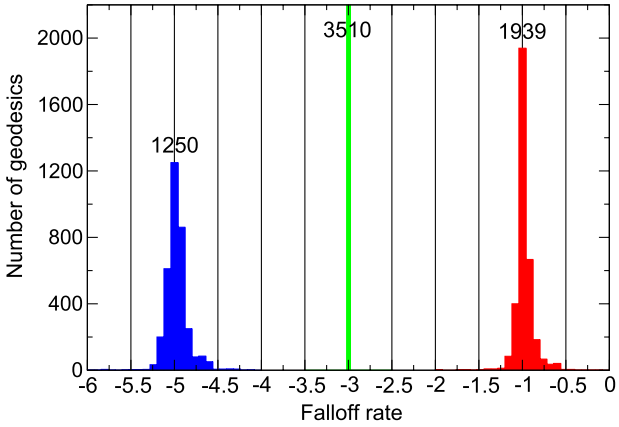

FIG. 11 (color online). The distribution of power-law falloff rates of Newman-Penrose scalars $\hat{\Psi}_i$ against affine parameter τ. The three concentrations (colored blue, green and red) from left to right indicate falloff rates of $\hat{\Psi}_0$, $\hat{\Psi}_2$ and $\hat{\Psi}_4$, respectively. The vertical axis indicates the number of geodesics (totaling 3510) with falloff rate falling inside bins of width 0.08, and the number of geodesics for the centermost bins are shown.

Recall that in fixing the spin-boost or type-III freedom of the QKF to obtain the QKT, the $\hat{l}$ vector was scaled so that $\hat{\Psi}_2 \propto (\hat{r})^{-3}$. The very sharply defined peak at -3 in Fig. 11 provides direct numerical evidence that the relation $\tau \propto \hat{r}$ (cf. Secs. III H and IV B) remains valid at leading order for the considered range of the computational domain.

Figure 11 also indicates that $|\hat{\Psi}_0|$ and $|\hat{\Psi}_4|$ scale as τ^{-5} and τ^{-1}, respectively, as expected from Eq. (3.48). Here, the peaks are not as sharply defined, since we do not by construction enforce the power-law scalings of $\hat{\Psi}_0$ and $\hat{\Psi}_4$ (as we do for $\hat{\Psi}_2$).

B. Head-on nonspinning binary merger

To further examine the properties of the QKT and the geometrical coordinates, we now take a detailed look at the numerical simulation of a head-on merger. The physical parameters of the simulation are given in Table II.

The axisymmetric head-on collision of two nonspinning black holes has been studied extensively [45–49]; in many respects, these collisions serve as a simple, strongly nonlinear test of numerical relativity codes. The existence of a twist-free azimuthal Killing vector on this spacetime implies that the metric does not explicitly depend on the azimuthal coordinate ϕ defined about the symmetry axis and that the angular momentum of the spacetime is zero. We note that because of the symmetry of this configuration, the Coulomb potential associated with the transverse frame is real and thus that only one geometric coordinate, the radial coordinate $\hat{r}$, can be determined from it. Therefore, we fix the latitudinal coordinate to the simulation coordinate θ.

TABLE II. Physical parameters of the head-on binary-black-hole merger considered in Sec. VI B. Here, M is the sum of the initial black hole Christodoulou masses, and all initial quantities are measured at the initial time $t = 0$ of the simulation.

Initial separation	$d/M = 20$
Initial spin of each hole	$S/M^2 \leq 2 \times 10^{-12}$
Duration of evolution	$\Delta T/M = 600$
Final black hole mass	$M_f/M = 0.987 \pm 2 \times 10^{-3}$
Final black hole spin	$S_f/M_f^2 = 3. \times 10^{-7} \pm 2 \times 10^{-7}$

1. Geometric radial coordinate

We now explore some of the properties of radial coordinate $\hat{r}$, the emitted radiation profile, and the waveform. We show contour plots of the $\hat{r}$ coordinate at various times near merger in Fig. 12. The characteristic peanut shape expected from the merger event is clearly visible, and surfaces of constant $\hat{r}$ coordinate trace both the individual apparent horizon surfaces at early times and the final apparent horizon surface at late times. Far from the source, constant $\hat{r}$ surfaces become roughly spherical, indicating that there the geometrical concept of radius and the gauge choice for the radial coordinate in the simulation coincide well. For the head-on collision, as well as in the more dynamical spacetimes depicted in Fig. 2, plotting surfaces of constant $\hat{r}$ turns out to be a useful tool for visualizing the

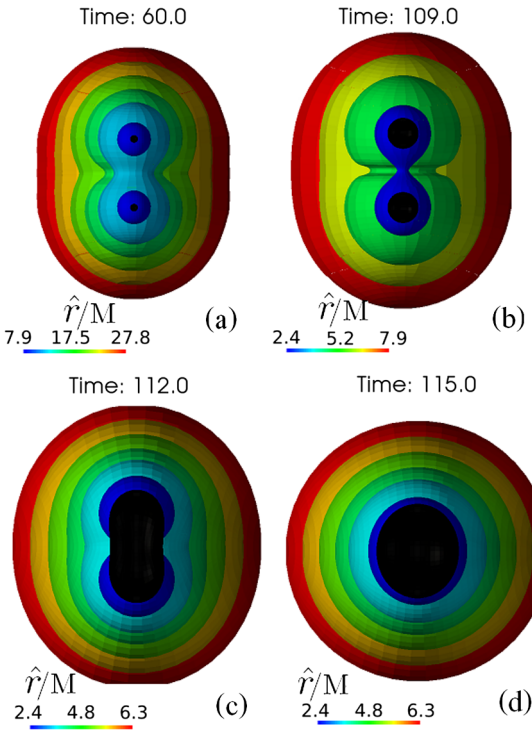

FIG. 12 (color online). Here, we show the evolution of $\hat{r}$ contours during the merger in the near zone; the black surfaces in these plots are the apparent horizons, and at $t = 112$ M, the common apparent horizon forms.

spacetime geometry in a way which corresponds to an intuitive feel of the Coulomb potential's behavior.

2. Gravitational waveform

For twist-free axisymmetric spacetimes, one can show in general [45] that if the imaginary part of the tetrad null vector $\boldsymbol{m}$ or $\boldsymbol{E}^3$ (as defined in Sec. II A) has the same direction as the azimuthal Killing vector, then Ψ_4 expressed on this tetrad is real. Figure 13 depicts $\Re(\hat{\Psi}_4)$ for the head-on collision presently under consideration. Note the absence of radiation along the symmetric axis in Fig 13; this is a feature we will examine further later in this section in the context of PNDs.

We show two possible spherical harmonic decompositions of $\hat{\Psi}_4$ in Fig. 14. Panel (a) corresponds to the case where the azimuthal Killing vector determines the $\theta = 0$ direction; because the symmetry-axis corresponds to the $\theta = 0$ direction, axisymmetry implies that there are no $l = 2$, $m = \pm 2$ modes in the spherical harmonic decomposition, only $m = 0$ modes exist, and of those, the $l = 2$, $m = 0$ mode makes the dominant contribution.

On the other hand, if one relabels the θ and ϕ coordinates on the extraction sphere, the spherical harmonic decomposition of the same waveform is very different. Panel (b) of Fig. 14 instead chooses the $\theta = 0$ line to be orthogonal to the axisymmetry axis rather than along it [as in panel (a)]; a significant $l = 2$, $m = 2$ mode appears. This is a simple example illustrating the well-known fact that unless a clear prescription for the preferred axis of a simulation is given, the $l = 2$, $m = 2$ mode is an ambiguous description of the radiation. Solutions to this problem for generic black-hole-binary simulations (which include precession) have been proposed in literature. For example, one may first choose a *radiation axis* [50,51] to maximize the component of the angular momentum along itself and, second, choose a preferred rotation about that axis [52]. Although not yet fully explored, our geometric coordinates suggest an alternative resolution; namely, that on the wave extraction sphere, Eq. (3.29) can be used to identify the term $\hat{a}\cos\hat{\theta}$ whose maximum and minimum values respectively identify the north and south pole regions of the sphere.

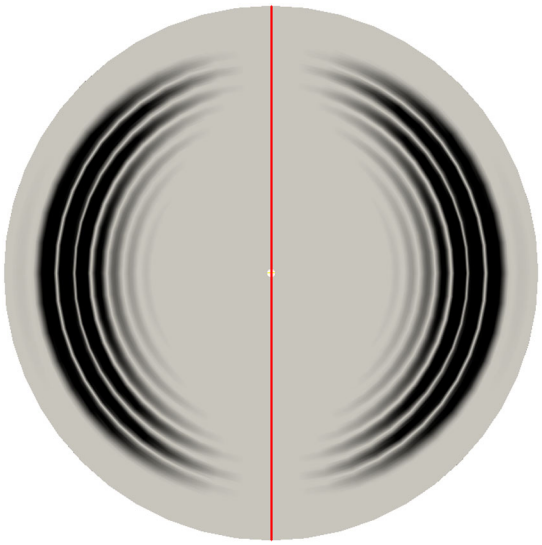

FIG. 13 (color online). A snapshot (at $t = 242.25$ M) of latitudinal distribution of radiation emitted by the head-on collision. The coloring is according to $|\Re(\hat{\Psi}_4)|$, with large values corresponding to darker color. The disk is a vertical slice of the computational domain with the thick red line denoting the symmetry axis.

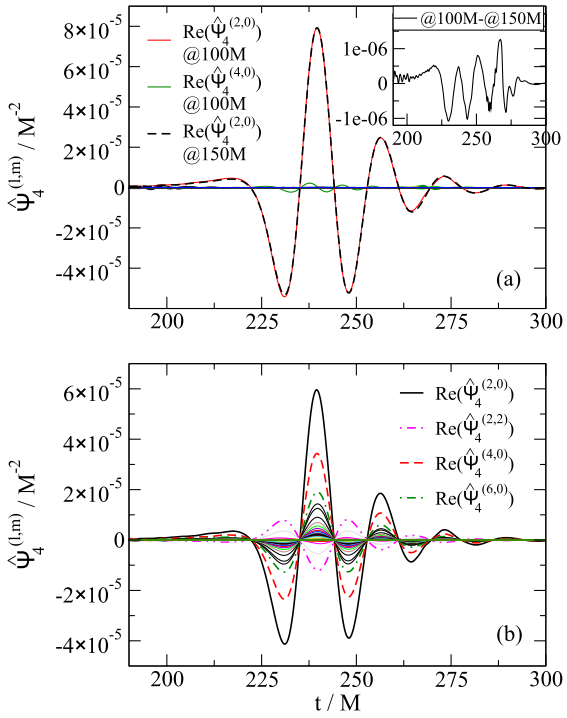

FIG. 14 (color online). (a) The $\hat{\Psi}_4$ waveform for the head-on simulation extracted at coordinate radii of $r = 100$ M and $r = 150$ M. For the waveform at $r = 100$ M, all ${}_{-2}Y_{lm}$ modes up to $l = 35$ are shown. Only $\Re(\hat{\Psi}_4^{(2,0)})$ and $\Re(\hat{\Psi}_4^{(4,0)})$ are discernibly nonvanishing, with the former clearly dominating. For the $r = 150$ M waveform, only $\Re(\hat{\Psi}_4^{(2,0)})$ is shown, and it is shifted temporally and rescaled by ≈ 1.5 so that its maximum peak location and magnitude match those of the $r = 100$ M waveform. The difference between the two waveforms is shown in the top-right inset. (b) The spherical harmonic decomposition for $\hat{\Psi}_4$ at $r = 100$ M obtained by choosing the poles of harmonics along a direction orthogonal to the symmetry axis. Multiple modes are visible, and a few with the largest magnitudes are labelled.

Another question especially relevant to wave extraction is how rapidly the waveform computed from $\hat{\Psi}_4$ in the computational domain converges to the correct asymptotic waveform. In Sec. III H, we argue that asymptotically the QKT quantities on the correct outgoing geodesics (as described in Sec. IV B) should converge very rapidly to the desired result. We now explore this

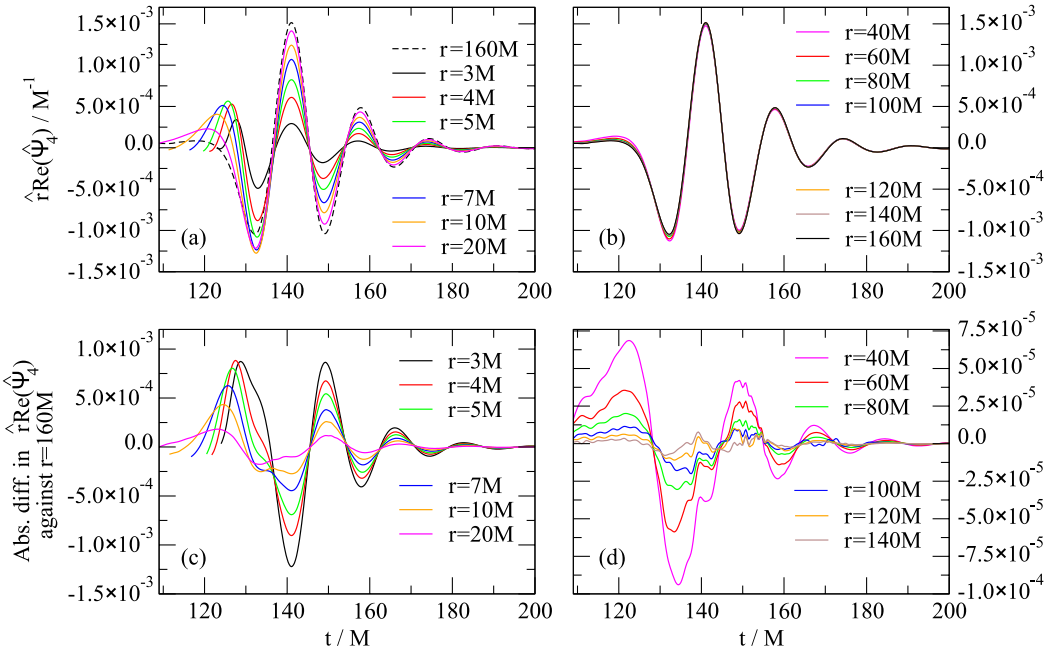

FIG. 15 (color online). Panels (a) and (b): The gravitational-wave signal $\hat{r}\Re(\hat{\Psi}_4)$ curves extracted at several fixed spatial (simulation) coordinates. Panels (c) and (d): The absolute difference between these waveforms with a reference waveform computed at $r = 160$ M.

statement quantitatively for the emitted radiation on the equatorial plane in the head-on binary-black-hole merger we are considering. The goal is to determine at which radius a reliable approximation of the asymptotic waveform is attained.

To locate a good cutoff radius for wave extraction, consider a set of noninertial observers hovering at different fixed spatial (simulation) radii in the equatorial plane. For each observer, in Fig. 15, we record the $\hat{r}\hat{\Psi}_4$ value as a function of time and plot the resulting curves, with the origin shifted so that the central maxima of all the curves coincide at around $t = 140$ M. For clarity, we have divided the curves into two sets, those originating at $r < 30$ M and at $r > 30$ M, which we display in panels (a) and (b), respectively. In both panels, the curve traced out at $r = 160$ M is given for comparison, and we will refer to it as the reference waveform. Panels (c) and (d) show the absolute difference between the curves extracted at the various interior points and the reference waveform.

In Fig. 16, we plot the fractional difference between reference waveform and the interior waveform as a function of extraction radius. The quantity plotted is the L_2 norm of the absolute difference between the two waveforms divided by the L_2 norm of the reference waveform. The L_2 norm is defined here as

$$L_2[f] = \sqrt{\int_{t=125}^{200} f^2(t)dt}. \tag{6.2}$$

Comparing Fig. 16 and panel (b) in Fig. 15, we find that for radii greater than $r = 40$ M, the extracted waveform corresponds closely, within ~5%, to the reference waveform. Figure 16 quantifies this further: for $r < 40$ M, the errors in the extracted $\hat{\Psi}_4$ waveform are large, but the convergence to the reference waveform is superexponential, while for $r > 40$ M, the errors converge exponentially. This provides quantitative justification for the rapid-convergence claims we made in Secs. III H with respect to the Newman-Penrose scalars calculated on the QKT. We conclude that the radius $\hat{r} = 40$ M appears to be a good

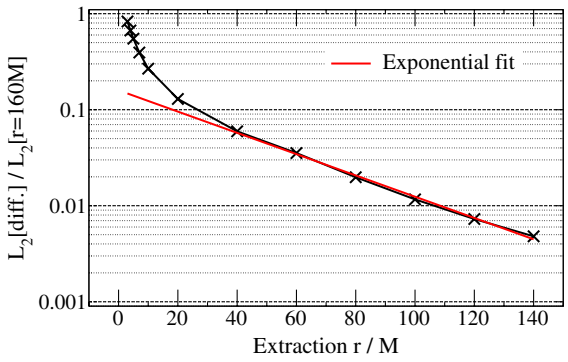

FIG. 16 (color online). Exponential convergence of the QKT waveform extracted in the interior to the reference waveform measured at $r = 160$ M. This plot shows the L_2 norm [defined in Eq. (6.2)] of the absolute difference between the waveform at a particular extraction radius and the reference waveform at $r = 160$ M normalized by dividing by the L_2 norm of the reference waveform. Also shown is the red fitted exponential curve for radii $r > 40$ M, which has a slope of -0.011.

minimal extraction radius for QKT quantities for head-on binary-black-hole collisions. It would be interesting to explore, using a similar analysis, whether the exponential convergence properties and the value for a good minimal extraction radius change considerably when applied to generic spacetimes (i.e., to spacetimes with less symmetry than the head-on collision we consider here).

3. Principal null directions

We conclude our investigation of the spacetime associated with the head-on collision of two black holes by exploring the behavior of the PNDs on and off the axis. As we have observed and shown graphically in Fig. 13, no radiation is emitted along the symmetry axis. This lack of radiation suggests that the PNDs do not all converge into a type-N pure radiation configuration as seen in Fig. 3(c); instead, we would expect the PNDs to remain in a type-D configuration, with two pairs of PNDs trapped at antipodal points of the anticelestial sphere. On the axis, the only nonvanishing Newman-Penrose scalar on the QKT is $\hat{\Psi}_2$. The four solutions in Eq. (3.54) then divide into a pair whose values diverge and a pair which approaches zero. The diverging solutions give us two PNDs pointing along the $\hat{\boldsymbol{n}}$ direction, while the vanishing solutions coincide with $\hat{\boldsymbol{l}}$. This situation is depicted in Fig. 17(a): the two PNDs at the bottom of the sphere point away from $\hat{\boldsymbol{l}}$ (represented by the radial line) and do not converge onto the other two PNDs which coincide with $\hat{\boldsymbol{l}}$ at the top of the anticelestial sphere. All the PNDs on the top of the sphere form angles smaller than $4 \times 10^{-7}\pi$ with the spatial projection of $\hat{\boldsymbol{l}}$, while the other two PNDs form angles with the spatial projection of $\hat{\boldsymbol{n}}$ which are smaller than $4 \times 10^{-6}\pi$. For comparison, in Fig. 17(b), we show the PND behavior on the celestial sphere as one moves along a geodesic which points away from the symmetry axis. The geodesic shown in this plot starts out at an orientation of 0.508π to the symmetry axis. (A similar plot is made in Fig. 3(c) where we showed a geodesic starting at 0.396π to the symmetry axis). In these two cases, the presence of radiation causes the two PNDs pointing away from $\hat{\boldsymbol{l}}$ to converge onto the other two PNDs surrounding $\hat{\boldsymbol{l}}$ as one moves outward along the geodesic. The dominant rate of convergence is $1/\tau$ [cf., Eq. (3.53)].

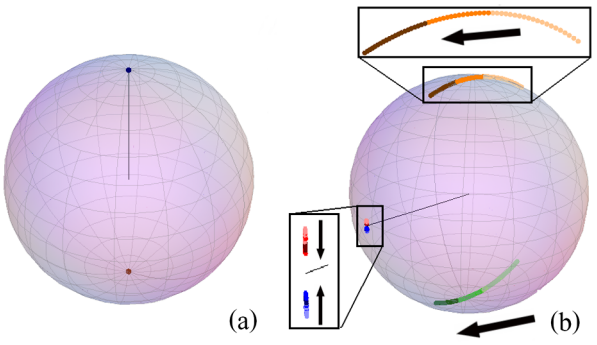

FIG. 17 (color online). A graphical representation of the peeling-off behavior of the PNDs along outgoing null geodesics for the head-on collision. The null geodesics start at $r = 30$M at time $t = 152$M. The tangent ℓ to the geodesics coincide with $\hat{\boldsymbol{l}}$ along the geodesic and is denoted in the figures by black radial lines. The geodesic shown in panel (a) travels outward along the symmetry axis where no gravitational radiation is emitted. The geodesic shown in panel (b) starts off near the equatorial plane, and all PNDs converge toward the outgoing $\hat{\boldsymbol{l}}$ direction pointing toward the front of the sphere. In this figure, the arrows indicate the movements of the PNDs as one travels further along the geodesic. Darker coloring indicates points calculated at larger affine parameter along the geodesic.

The existence of *critical* directions as demonstrated here in the special case of axisymmetric spacetimes is a generic feature of all dynamical spacetimes: it is a topological necessity (see Ref. [53] and page 173 of Ref. [34]). Specifically, in Ref. [53], the authors explain this feature as follows: In the asymptotic region, gravitational radiation is transverse and can be represented by tendex and vortex lines tangent to spheres of constant $\hat{r}$. Then, the Poincaré-Hopf theorem dictates that there must be locations on the sphere where the tendicity associated with the two transverse eigenbranches of the gravitoelectric tensor $\boldsymbol{\mathcal{E}}$ become degenerate. The trace-free property of $\boldsymbol{\mathcal{E}}$ then further constrains the tendicity to be zero—i.e., requires the gravitational radiation to vanish at the critical points.

Another useful characterization of dynamical numerical simulations is a measure of how rapidly the spacetime settles down to Petrov type D at late times (see for example Refs. [54,55]). As a graphic depiction of this evolution of spacetime, one may generate PND diagrams similar to Fig. 17 along timelike world lines (instead of null geodesics). If one desires a quantitative estimate of the rate at which this *settling down* occurs, a metric on the anticelestial sphere has to be defined in order to calculate distance between the PNDs. However, a unique prescription of this metric requires a unique prescription of the tetrad, since Lorentz transformations on tetrad result in conformal transformations on the anticelestial sphere. The QKT construction is useful in this context, because it uniquely prescribes all the tetrad degrees of freedom simultaneously across spacetime, including along timelike world lines.

VII. CONCLUSION

As the numerical relativity codes mature, it is becoming increasingly important to introduce a protocol which allows us to extract and compare physics from these codes in an unambiguous fashion. In particular, the quantities computed should be independent of the gauge or the formulation used. Ideally, such a protocol should be valid in the strong field and wave zones and meet the physical criteria outlined in Sec. III.

In this paper, we have suggested one such approach. Based on the Newman-Penrose formalism, our method

fully specifies the tetrad degrees of freedom using purely geometric considerations, and two of the gauge degrees of freedom are also uniquely fixed using the curvature invariants I and J. In particular, our tetrad construction makes use of the quasi-Kinnersley frame [9–13], which is a transverse frame which contains the Kinnersley tetrad in the Kerr limit.

By exploiting the relationship between QKF and eigenvectors of the matrix representation $\mathcal{Q}$ [as in Eq. (2.12)] of the Weyl tensor, one can arrive at several insights regarding the physical properties of the QKF: i) Its null vector $\tilde{l}$ has a spatial projection pointing along the super-Poynting vector (Sec. III A) and thus along the direction of wave propagation, and ii) there is (Sec. III H) a close relationship [Fig. 3(b)] between the QKF null basis and principal null directions which makes the QKF naturally suited to measuring how quickly PNDs bunch together (as they converge onto $\tilde{l}$). These features help Newman-Penrose scalars extracted using a QKT to fall off correctly in accordance with predictions by the peeling theorem.

In the QKF, the eigenvalue $\hat{\Psi}_2$ of the complex matrix $\mathcal{Q}$ corresponding to the eigenvector which gave us QKF is a curvature invariant thus independent of the slicing in which the calculation was performed. The physical interpretation of $\hat{\Psi}_2$ is that it represents the Coulomb background portion of Weyl tensor; using this quantity, we define a pair of geometric coordinates $\hat{r}$ and $\hat{\theta}$ (Sec. III D). These geometric coordinates vividly depict the multipolar structure in the Coulomb potential (as can be seen from Figs. 10 and 12). For example, they were used to demonstrate that far enough away from their source (see Sec. VI B for an empirical cutoff), the Coulomb background $\hat{\Psi}_2$ (Fig. 10) appears to propagate with an almost invariant form along preferred characteristic surfaces whose generators are geodesics started off in the QKT $\hat{l}$ direction. Besides fixing the gauge freedom, we have also used the differentials $d\hat{r}$ and $d\hat{\theta}$ (Sec. III E) to eliminate the spin-boost freedom remaining in QKF, yielding a final, gauge-invariant quasi-Kinnersley tetrad.

As our QKT is constructed from the gauge-invariant characteristic structure of Weyl tensor, it can be used to explore the physical features of numerical spacetimes in a gauge-invariant way. We have demonstrated this desirable property of our QKT with i) a stationary black-hole spacetime where the hole is offset from the origin (Sec. V A 1) as well as ii) a gauge wave (Sec. V A 2) or iii) physical wave (Sec. V B) added to the spacetime of a Schwarzschild black hole. These examples serve as useful test beds for codes seeking to unambiguously extract the physically real effects as opposed to gauge induced false signals.

We have also used the QKT to analyze two equal-mass, nonspinning binary-black-hole merger simulations. In the first, the two black holes inspiral (Sec. VI A) toward each other, while in the second, they plunge head-on (Sec. VI B). We have confirmed that the Newman-Penrose scalars under the QKT do indeed fall off at the rates expected from peeling theorem in these simulations (Fig. 11 and 15), and we have explicitly examined the special peeling behavior along critical directions whose existence is ensured by topology (Fig. 17).

The gauge-invariant feature of the proposed framework lends itself to several uses. One possible application is that they could help eliminate ambiguities such as the pole direction of harmonics used to express gravitational waves (see Sec. VI B 2). A further application is to use the QKT to reduce the ambiguity in measuring how quickly a spacetime settles down to a type-D spacetime (see the end of Sec. VI B). The QKT also is promising as a wave extraction method which can be performed in real time and ensures that waveform approaches its asymptotic value at infinity as rapidly as possible (this is illustrated in Fig. 15). For future work, we plan to make a comparison between QKT-based wave extraction and other wave -extraction techniques (such as Cauchy characteristic extraction [56–61]) using various numerical simulations with generic initial conditions.

The validity of geometric coordinates and the QKT throughout spacetime, including the strong field regions, suggests that they could be effectively utilized as a visualization and diagnostic tool capable of tracking the evolution of dynamical features of the spacetime. For example, in Fig. 4(a), the geometric coordinates point out the missing rotating quadrupolar moment in the initial data. We expect this type of visualization to prove valuable in ongoing efforts to construct more realistic initial data and reduce spurious junk radiation. Other utilities for the geometric coordinates include, e.g., their potential for helping to improve boundary matching algorithms [see Fig. 4(b)]. We would further like to examine in greater depth, with the help of QKT, the mechanics behind the changes in waveform, as one moves closer to the source region (see Fig. 15).

Finally, we note that there should exist a close relationship between the QKT and the tendex and vortex infrastructure introduced in Refs. [16,17], which is based on the real eigenvectors and eigenvalues of $\mathcal{E}$ and $\mathcal{B}$. Our geometric coordinates and QKT are, in contrast, based on the complex eigenvalues and eigenvectors of $\mathcal{Q}$. We expect this connection to yield important insights, for example, regarding the slicing dependence of the tendexes and vortexes.

ACKNOWLEDGMENTS

We would like to thank Luisa Buchmann for alerting the NR group at Caltech about the potential of the QKTs to aid wave extraction, and we are indebted to Andrea Nerozzi and Rob Owen for many useful discussions and to Mark Scheel for numerous assistance with the SpEC code. This research was supported by NSF Grants

No. PHY-1068881 and No. PHY-1005655 at Caltech and by NSF Grants No. PHY-0969111, No. PHY-1005426 at Cornell, by NASA Grants No. NNX09AF97G and No. NNX09AF96G, and by the Sherman Fairchild Foundation to Caltech and Cornell and the Brinson Foundation to Caltech. The numerical computations in this paper were completed using the Caltech computer cluster ZWICKY, which was funded by the Sherman Fairchild Foundation and the NSF MRI-R2 Grant No. PHY-0960291 to Caltech.

[1] J. Centrella, J. G. Baker, B. J. Kelly, and J. R. van Meter, Rev. Mod. Phys. **82**, 3069 (2010).
[2] S. T. McWilliams, Classical Quantum Gravity **28**, 134001 (2011).
[3] B. C. Barish and R. Weiss, Phys. Today **52**, No. 10, 44 (1999), .
[4] D. Sigg and the (LIGO Scientific Collaboration), Classical Quantum Gravity **25**, 114041 (2008).
[5] F. Acernese *et al.*, Classical Quantum Gravity **23**, S635 (2006).
[6] K. Kuroda and the (LCGT Collaboration), Classical Quantum Gravity **27**, 084004 (2010).
[7] casa.colorado.edu/ ajsh/phys5770_10/grtetrad.pdf.
[8] W. Kinnersley, J. Math. Phys. (N.Y.) **10**, 1195 (1969).
[9] C. Beetle, M. Bruni, L. M. Burko, and A. Nerozzi, Phys. Rev. D **72**, 024013 (2005).
[10] A. Nerozzi, C. Beetle, M. Bruni, L. M. Burko, and D. Pollney, Phys. Rev. D **72**, 024014 (2005).
[11] L. M. Burko, T. W. Baumgarte, and C. Beetle, Phys. Rev. D **73**, 024002 (2006).
[12] A. Nerozzi, M. Bruni, V. Re, and L. M. Burko, Phys. Rev. D **73**, 044020 (2006).
[13] L. M. Burko, Phys. Rev. D **75**, 084039 (2007).
[14] M. Campanelli, B. Kelly, and C. O. Lousto, Phys. Rev. D **73**, 064005 (2006).
[15] S. Chandrasekhar, *The Mathematical Theory of Black Holes* (Oxford University Press, Oxford, 1983).
[16] D. A. Nichols, R. Owen, F. Zhang, A. Zimmerman, J. Brink, Y. Chen, J. Kaplan, G. Lovelace, K. D. Matthews, M. A. Scheel *et al.*, Phys. Rev. D **84**, 124014 (2011).
[17] R. Owen, J. Brink, Y. Chen, J. D. Kaplan, G. Lovelace, K. D. Matthews, D. A. Nichols, M. A. Scheel, F. Zhang, A. Zimmerman *et al.*, Phys. Rev. Lett. **106**, 151101 (2011).
[18] K. A. Dennison and T. W. Baumgarte, arXiv:1207.2431.
[19] F. B. Estabrook and H. D. Wahlquist, J. Math. Phys. (N.Y.) **5**, 1629 (1964).
[20] C. Schmid, Phys. Rev. D **79**, 064007 (2009).
[21] J. Carminati and R. McLenaghan, J. Math. Phys. (N.Y.) **32**, 3135 (1991).
[22] P. T. Chrusciel, Contemp. Math. **170**, 23 (1994).
[23] M. Heusler, Living Rev. Relativity **1**, 6 (1998).
[24] S. Teukolsky, Phys. Rev. Lett. **29**, 1114 (1972).
[25] R. Penrose and W. Rindler, *Spinors and Space-time* (Cambridge University Press, Cambridge, England, 1986), Vol. 2.
[26] P. Szekeres, J. Math. Phys. (N.Y.) **6**, 1387 (1965).
[27] R. Maartens and B. A. Bassett, Classical Quantum Gravity **15**, 705 (1998).
[28] V. Zakharov, *Gravitational Waves in Einstein's Theory* (Halsted Press, New York, 1973).
[29] P. Anninos, D. Hobill, E. Seidel, L. Smarr, and W.-M. Suen, Phys. Rev. D **52**, 2044 (1995).
[30] J. G. Baker and M. Campanelli, Phys. Rev. D **62**, 127501 (2000).
[31] R. Sachs, Proc. R. Soc. A **264**, 309 (1961).
[32] R. K. Sachs, Proc. R. Soc. A **270**, 103 (1962).
[33] R. Penrose, Phys. Rev. Lett. **10**, 66 (1963).
[34] R. Penrose, Proc. R. Soc. A **284**, 159 (1965).
[35] http://www.black-holes.org/SpEC.html.
[36] H. Friedrich, Classical Quantum Gravity **13**, 1451 (1996).
[37] J. Hesthaven and T. Warburton, *Nodal Discontinuous Galerkin Methods: Algorithms, Analysis, and Applications* (Springer-Verlag, New York, NY, 2008).
[38] N. W. Taylor, L. E. Kidder, and S. A. Teukolsky, Phys. Rev. D **82**, 024037 (2010).
[39] L. Lindblom, K. D. Matthews, O. Rinne, and M. A. Scheel, Phys. Rev. D **77**, 084001 (2008).
[40] F. Pretorius, Phys. Rev. Lett. **95**, 121101 (2005).
[41] F. Pretorius, Classical Quantum Gravity **23**, S529 (2006).
[42] L. Lindblom and B. Szilágyi, Phys. Rev. D **80**, 084019 (2009).
[43] O. Sarbach and M. Tiglio, Phys. Rev. D **64**, 084016 (2001).
[44] M. A. Scheel, M. Boyle, T. Chu, L. E. Kidder, K. D. Matthews, and H. P. Pfeiffer, Phys. Rev. D **79**, 024003 (2009).
[45] D. R. Fiske, J. G. Baker, J. R. van Meter, D.-I. Choi, and J. M. Centrella, Phys. Rev. D **71**, 104036 (2005).
[46] M. Alcubierre, B. Bruegmann, P. Diener, F. Herrmann, D. Pollney *et al.*, arXiv:gr-qc/0411137.
[47] U. Sperhake, B. Kelly, P. Laguna, K. L. Smith, and E. Schnetter, Phys. Rev. D **71**, 124042 (2005).
[48] J. G. Baker, B. Bruegmann, M. Campanelli, and C. O. Lousto, Classical Quantum Gravity **17**, L149 (2000).
[49] J. G. Baker, M. Campanelli, C. O. Lousto, and R. Takahashi, Phys. Rev. D **65**, 124012 (2002).
[50] P. Schmidt, M. Hannam, S. Husa, and P. Ajith, Phys. Rev. D **84**, 024046 (2011).
[51] R. O'Shaughnessy, B. Vaishnav, J. Healy, Z. Meeks, and D. Shoemaker, Phys. Rev. D **84**, 124002 (2011).
[52] M. Boyle, R. Owen, and H. P. Pfeiffer, Phys. Rev. D **84**, 124011 (2011).
[53] A. Zimmerman, D. A. Nichols, and F. Zhang, Phys. Rev. D **84**, 044037 (2011).
[54] M. Campanelli, C. O. Lousto, and Y. Zlochower, Phys. Rev. D **79**, 084012 (2009).

[55] R. Owen, Phys. Rev. D **81**, 124042 (2010).
[56] N. T. Bishop, R. Gómez, L. Lehner, and J. Winicour, Phys. Rev. D **54**, 6153 (1996).
[57] N. T. Bishop, R. Gomez, L. Lehner, M. Maharaj, and J. Winicour, Phys. Rev. D **56**, 6298 (1997).
[58] N. T. Bishop, R. Gómez, R. A. Isaacson, L. Lehner, B. Szilágyi, and J. Winicour, in *Black Holes, Gravitational Radiation and the Universe*, edited by B. R. Iyer and B. Bhawal (Kluwer, Dordrecht, 1998), Chap. 24.
[59] C. Reisswig, N. T. Bishop, D. Pollney, and B. Szilagyi, Classical Quantum Gravity **27**, 075014 (2010).
[60] J. Winicour, Living Rev. Relativity **12** (2009).
[61] M. C. Babiuc, B. Szilágyi, J. Winicour, and Y. Zlochower, Phys. Rev. D **84**, 044057 (2011).